



Atomistic modeling of pulsed laser ablation in liquid: spatially and time-resolved maps of transient nonequilibrium states and channels of nanoparticle formation

Chaobo Chen¹ · Leonid V. Zhigilei¹

Received: 30 December 2022 / Accepted: 22 February 2023

© The Author(s), under exclusive licence to Springer-Verlag GmbH, DE part of Springer Nature 2023

Abstract

The mechanisms of picosecond pulse laser ablation in liquid are investigated in a series of large-scale atomistic simulations performed for FeNi targets irradiated in a liquid environment by picosecond laser pulses at a broad range of fluences. The simulations reveal the existence of three fluence regimes featuring different dominant mechanisms of material ejection and nanoparticle formation. These are (1) the low fluence regime, where atomic clusters and small nanoparticles form through the evaporation of metal atoms followed by condensation in a low-density region at the front of the ablation plume, (2) the medium fluence regime, where roughening and decomposition of a top part of a transient spongy structure of interconnected liquid regions leads to the formation of large nanoparticles, and (3) the high fluence regime, where the nanoparticles form primarily at the phase separation front propagating through the ablation plume cooled from the supercritical state by expansion against the liquid environment and mixing with the liquid. The generation of the largest nanoparticles is observed in the medium fluence regime, and both the maximum size of the nanoparticles and the energy efficiency of the material conversion into nanoparticles decrease upon transition to the high fluence regime. Some of the nanoparticles experience extreme quench rates and rapidly solidify under conditions of deep undercooling, yielding a population of defect-rich nanoparticles of interest for practical applications. The results of the simulations are mapped to the conditions realized within a laser spot irradiated by a beam with a Gaussian spatial profile, where different ablation regimes are activated simultaneously in different parts of the laser spot. The spatially and time-resolved maps of the transient nonequilibrium states predicted in the simulations provide a comprehensive picture of the ablation dynamics and a solid foundation for interpretation of the results of time-resolved experimental probing of the initial stage of the ablation process.

Keywords Pulsed laser ablation in liquids · Nanoparticles · Atomistic simulations · Molecular dynamics · Nucleation and growth · Spinodal decomposition · Phase explosion · Gaussian laser beam

1 Introduction

The widespread and rapidly expanding utilization of nanoparticles (NPs) in catalysis [1, 2] manufacturing of advanced materials [3–7], solar energy conversion [8, 9], and biomedical applications [10–13] is defining the need for accelerated development of advanced NP synthesis techniques capable of meeting the sharp rise in the global demand. Synthesis

of nanoparticles (NPs) by pulsed laser ablation in liquids (PLAL) is a well-established environment-friendly “green” technique [14, 15] capable of producing large quantities of NPs at a cost competitive with chemical synthesis [16].

The highly nonequilibrium conditions of NP synthesis in PLAL, characterized by ultrafast quench rates and growth under extreme supersaturation, can lead to the formation of NPs featuring high densities of crystal defects and metastable phases. Indeed, atomistic simulations of PLAL of metal targets [17, 18] suggest that NPs experiencing fast cooling rates in the process of their formation tend to exhibit high densities of twin boundaries and stacking faults. The experimental HRTEM characterization of metal NPs produced by PLAL confirms the presence of planar defects [19–21] and metastable phases [22]. The unique internal structures of

✉ Leonid V. Zhigilei
lz2n@virginia.edu

¹ Department of Materials Science and Engineering,
University of Virginia, 395 McCormick Road,
Charlottesville, VA 22904-4745, USA

NPs synthesized by PLAL make them particularly attractive in many applications. In particular, it is recognized that the presence of crystal defects and strain in NP catalysts substantially enhances their catalytic activity [19–21, 23], while the phase composition of NPs may affect their magnetic properties [22].

Tuning the characteristics of NPs produced by PLAL to the needs of practical applications, however, still presents a significant challenge and calls for detailed analysis of processes defining the size distribution and internal structure of the NPs. The results of time-resolved experimental probing [24–29] and computational modeling of PLAL [17, 18, 30–37] provide strong evidence in favor of the coexistence of multiple channels of the NP formation activated at different stages of laser ablation and producing distinct populations of NPs. The processes occurring on the timescale of the cavitation bubble expansion and collapse (10^{-6} – 10^{-4} s) have been the focus of the majority of studies of PLAL, where the nucleation, growth, and coalescence of NP inside the cavitation bubble [24–27, 38–40], as well as the mechanical impact due to the cavitation bubble collapse [41, 42], have been considered. The results of large-scale atomistic simulations of PLAL of metal targets [17, 18, 31–37] indicate, however, that processes occurring at the initial dynamic stage of laser ablation, during the first nanoseconds after the laser irradiation, also play a critical role in the generation of NPs.

The simulations reveal that rapid deceleration of the ablation plume by the liquid environment leads to the formation of a dense and hot transient layer of the ablated material at the plume-liquid interface [17, 18, 32]. The interaction of this interfacial layer with the liquid environment brings the liquid to the supercritical state and activates three distinct channels of NP formation. First, the formation of a low-density region at the front of the emerging cavitation bubble, just above the hot transient layer, creates conditions amenable to rapid nucleation and growth of atomic clusters and small NPs from atoms that are continuously evaporating from the hot interfacial layer. Second, the interfacial layer itself is observed to roughen and eventually disintegrate into large molten droplets [17, 18, 31, 32, 34, 35] due to the development of hydrodynamic instabilities (Rayleigh–Taylor and Richtmyer–Meshkov) at the decelerated plume-liquid interface [18]. Some of these droplets are injected into the cold liquid environment outside the boundary of the cavitation bubble, cool rapidly, and solidify into defect-rich NPs [17, 18]. The disintegration of the interfacial layer lets the supercritical liquid stream down and mix with the lower part of the ablation plume, triggering the third mechanism of the NP formation—the spinodal decomposition of the plume cooled from the supercritical state by a combined effect of the plume expansion and mixing with the liquid [32].

While the direct experimental verification of the complex picture of the initial dynamic stage of PLAL predicted in

the simulations still presents a significant challenge, there is substantial indirect evidence supporting the computational predictions. The coexistence of several mechanisms of NP formation at the initial stage of the ablation process is consistent with broad and often bimodal NP size distributions commonly observed in PLAL experiments [17, 43–46]. Moreover, the formation of large (tens of nm) NPs at and beyond the boundary of the emerging cavitation bubble, predicted in the simulations, has been confirmed in double-pulse cavitation bubble imaging experiments [17], where small satellite bubbles surrounding the main cavitation bubble are demonstrated to contain NPs absorbing the energy of the second pulse. The notion of NPs serving as sources of the satellite bubbles is supported by imaging of cavitation bubbles generated in nanosecond PLAL performed in a multi-pulse irradiation regime, where the satellite bubbles formed around NPs generated by prior pulses are identified as a major factor defining the laser shielding effect [47]. The time-resolved X-ray diffraction probing of Au and Ag NPs generated in picosecond PLAL [28] not only detects the presence of large NPs outside the cavitation bubble at 4–5 μ s after the laser pulse but also reveals the crystalline nature of these NPs. In good agreement with the computational predictions [17, 18], the NPs with largest crystalline domains (15–20 nm) are detected at the front (and outside) of the expanding cavitation bubble.

The direct experimental evidence of the prompt (within the first nanoseconds after the laser irradiation), generation of NPs at the front of the ablation plume confined by the liquid environment has been obtained in recent time- and spatially resolved optical imaging of Au targets irradiated in water [29]. The variation of reflectivity within the irradiated spot can be interpreted in terms of the formation of a layer of ablated material at the plume-liquid interface, followed by the disintegration of the layer into large liquid droplets. The mapping of the rapid changes of the reflectivity within the laser spot to the variations of thermodynamic parameters and three-dimensional morphology of the matter undergoing highly nonequilibrium phase transformations, however, is far from being straightforward and calls for a close integration of the experimental, theoretical, and computational efforts [37].

To facilitate the integration of modeling and experiments, in the present paper we perform a detailed analysis of the temporal and spatial evolution of material density, temperature, and phase state within the whole laser spot based on the results of large-scale atomistic simulations of PLAL of a FeNi target. The choice of the target material is defined by the practical importance of this solid solution alloy as well as the strong localization of the laser energy deposition defined by the relatively low thermal conductivity and strong electron–phonon coupling. The localization of laser energy deposition makes it possible to simulate ablation with

smaller computational systems, which reduces the computational cost of atomistic simulations. The thermodynamic maps obtained in the simulations provide a solid foundation for the interpretation of the results of experimental probing of the initial stage of the ablation process and identification of the temporally and spatially-resolved activation of several distinct mechanisms of the NP formation.

2 Computational model

Large-scale atomistic modeling has been successfully applied for the investigation of highly nonequilibrium dynamic processes responsible for laser-induced surface modification [48, 49], ablation, and nanoparticle generation [17, 18, 31–37] in a liquid environment. Yet, due to the computational limitations, it is not feasible to directly model processes occurring within the whole laser spot in a single atomistic simulation. Indeed, for a typical diameter of a well-focused laser beam in tens of micrometers and the depth affected by the laser-induced structural and phase transformations in hundreds of nanometers, the number of atoms that must be considered in a simulation of laser ablation of a metal target exceeds 10^{13} . While this number is comparable to those of the record-setting molecular dynamic (MD) simulations [50], the numbers of atoms in the largest atomistic simulations addressing real physical phenomena

are several orders of magnitude smaller [51, 52]. Thus, the effect of the variation of laser fluence within the laser spot is commonly neglected in MD simulations of laser ablation. Nevertheless, the variation of deposited energy density across the irradiated spot due to the spatial inhomogeneity of the majority of laser beams can have important implications for the overall ablation dynamics and generation of NPs. Different processes can be expected to proceed simultaneously in different parts of a laser spot and collectively contribute to the ablation yield and the NP generation. To account for the variation of the laser energy deposition within a laser spot, we adopt a “mosaic” approach illustrated in Fig. 1, where the simulations performed at a range of laser fluences are mapped to different regions of the laser spot [53]. The laser beam is assumed to have a Gaussian spatial profile, and the individual simulations are performed for local fluences ranging from those below the ablation threshold at the periphery of the laser spot to the ones that lead to the explosive phase decomposition (“phase explosion” [54–56]) or transformation to the supercritical state of a surface region of the target in the central part of the laser spot.

The individual simulations are performed with a computational setup schematically illustrated in the right panel of Fig. 1. The computational domain consists of three distinct regions dynamically coupled to each other. In the first and main region, the processes of laser excitation of the metal target, laser-induced phase transformations, ablation, and

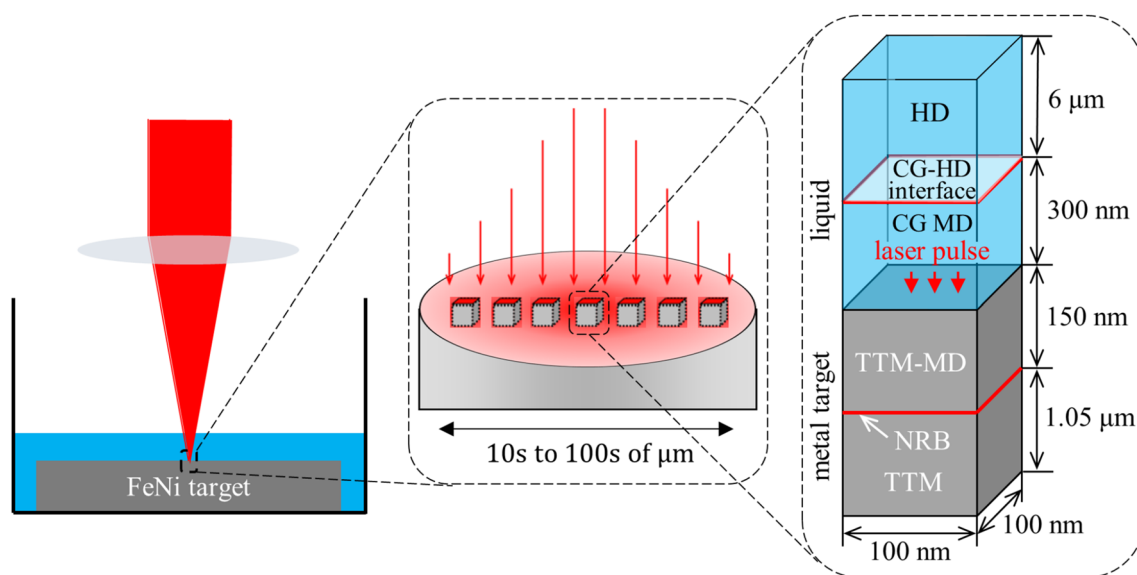


Fig. 1 Schematic diagram of the “mosaic” approach to the atomistic modeling of PLAL at the scale of the whole laser spot. A typical experimental setup in PLAL and an enlarged view of the laser spot are shown in the left and middle panels, respectively. The small boxes in the middle panel represent local volumes considered in large-scale atomistic simulations. A schematic of the initial system used in the atomistic simulations is provided in the right panel. The top part of

the metal target is represented by the TTM-MD model. The liquid environment is simulated with CG MD model in the vicinity of the target and with compressible HD model further away from the target. The non-reflecting propagation of the laser-induced stress wave into the bulk of the target is reproduced by an acoustic impedance matching boundary condition denoted as NRB. The heat conduction in the deeper part of the irradiated target is described by TTM equations

NP formation are simulated with a hybrid model that combines atomistic MD description of the metal target [53, 57] with a coarse-grained (CG) MD representation of the liquid environment [31]. The processes of the laser excitation of conduction-band electrons, electron–phonon coupling, and electron heat conduction are incorporated into the framework of the classical MD method by combining it with the two-temperature model (TTM) commonly used in the simulations of ultrashort pulse laser interactions with metals [58]. The TTM-MD + CG MD region is dynamically coupled to two much larger regions where continuum-level treatments of processes that do not involve structural and phase transformations are used. At the bottom of the computational domain, the heat transfer to the bulk of the irradiated metal target is represented by the TTM model, and the nonreflecting propagation of the laser-induced pressure waves through the boundary between the TTM-MD and TTM regions is ensured by the acoustic impedance matching nonreflecting boundary condition (NRB) [59]. At the top of the computational domain, the CG MD representation of the liquid environment is coupled to the compressible hydrodynamic (HD) model that provides a computationally efficient description of the long-term evolution of laser-induced shock waves in the liquid environment as well as the feedback of the surrounding liquid region to the behavior of the emerging cavitation bubble modeled with atomistic and coarse-grained MD.

Since detailed descriptions of the TTM-MD model for laser interactions with metal targets and CG MD model for the liquid environment are provided in Refs. [53, 57] and [31, 60, 61], respectively, below we only provide the parameters of the model relevant to the simulations reported in this paper. The simulations are performed for a FeNi target with equiatomic composition ($\text{Fe}_{50}\text{Ni}_{50}$). The temperature dependences of parameters of the TTM equation for the electron temperature (electron–phonon coupling factor, electron heat capacity and thermal conductivity) are taken in the forms that account for the thermal excitation from the electron states below the Fermi level [62–64] and reproduce experimental temperature and phase state (solid vs. liquid) dependence of the thermal conductivity under condition of electron–phonon thermal equilibrium ($T_e = T_l$) [64].

The interatomic interactions in the MD part of the TTM-MD model are described by the embedded atom method (EAM) potential parametrized by Bonny et al. [65]. This interatomic potential is designed to reproduce defects formation energy and mechanical properties of FeNiCr solid solution alloy system [65], and is found to provide a reasonable description of high-temperature properties of $\text{Fe}_{50}\text{Ni}_{50}$ alloy relevant to the investigation of laser-induced phase transformations [64]. In particular, the melting temperature T_m calculated for NiFe in liquid–crystal coexistence simulations is found to be 1680 K, very close to the experimental value

of 1703 K [66]. The thermodynamic critical temperature T_c of 4837 K is calculated by fitting the results of liquid–vapor coexistence simulations to a theoretical equation of state [67], using an approach described in Ref. [32]. This critical temperature of the alloy is 19% and 23% lower than the values estimated from experimental vapor pressure data for pure Fe and Ni, respectively [68].

The liquid environment is represented by the CG MD model [31, 60, 61] in the vicinity of the irradiated target and by the HD model further away from the target. The CG MD model uses a heat bath approach that associates an internal energy variable with each CG particle, which makes it possible to account for the dynamic degrees of freedom that are not explicitly present in the CG MD model. The capacity of the internal heat bath associated with each CG particle, its mass, and the parameters of interparticle interaction potential are fitted to the properties of water [60]. The model has been found to provide a reasonable semi-quantitative description of the aqueous environment, with the experimental density and heat capacity of water reproduced exactly, while other relevant properties, such as the speed of sound, bulk modulus, viscosity, surface energy, melting temperature, critical temperature, and critical density, do not deviate from the experimental values for water by more than 25% [31, 60].

The metal–liquid cross-interactions are described by the Lennard–Jones (LJ) potential. The energy parameter ϵ of the LJ potential is fitted to reproduce metal–water interfacial energies evaluated as described in Ref. [69] using the surface tension of water [70] and wetting angles measured for Ni [71] and Fe [72] surfaces. The length parameter σ of the LJ potential is chosen so that the equilibrium interparticle distance is the average of those in CG water [60] and metals [73]. This fitting yields $\sigma = 2.321 \text{ \AA}$ and $\epsilon = 32 \text{ meV}$ for Fe–CG particle interaction and $\sigma = 2.282 \text{ \AA}$ and $\epsilon = 9 \text{ meV}$ for Ni–CG particle interaction. The oxidation and other chemical reactions are not included in the model, as the chemical reactions are not expected to be prominent during the first nanoseconds of the ablation process considered in the simulations. At this early stage of PLAL, the oxidation may only occur at the very front of the ablation plume, in the liquid–plume mixing region, while the rest of the ablated material has not yet come into direct contact with the liquid environment. The notion of the limited effect of oxidation at the initial stage of PLAL is supported by the results of recent time-resolved synchrotron X-ray absorption spectroscopy probing of the generation of NPs in PLAL of Zn in water, where the NPs present in the cavitation bubble are found to exhibit metallic character with no detectable oxidation even at 100 μs after the laser pulse [74].

The liquid environment outside the region where the plume–liquid interaction takes place and the cavitation bubble appears is represented by a compressible HD model

dynamically coupled to the CG MD. The implementation of the HD model is based on one-dimensional Euler equations for mass, momentum, and energy transport solved with the Lax–Wendroff scheme [75]. The boundary cells of the HD spatial discretization overlap with the CG MD region, and the values of velocity, density, and energy predicted by MD are averaged with the ones predicted by the HD model. A plane is set as the boundary for MD, and the pressure and velocity at this plane are controlled by forces acting from both the MD and HD parts of the model. The equation of state for the HD model is fitted to the one predicted in CG MD simulations to get a consistent representation of properties of the liquid environment by the CG MD and HD parts of the combined model. Compared to the simple NRB condition applied at the top of the CG-MD region in earlier atomistic simulations of PLAL [17, 18, 31, 32, 34, 35], coupling the CG MD to the HD model not only enables direct tracking of the nonlinear shock wave propagation in the liquid environment [29, 41, 76] but also provides a more reliable representation of the inertial motion of liquid driven by the ablation process and a more realistic feedback of the surrounding liquid region to the behavior of the expanding cavitation bubble modeled with atomistic and coarse-grained MD.

The laser energy deposition is described by a source term added to the TTM equation for the electron temperature [57]. The source term has a Gaussian temporal profile with full width at half maximum of 10 ps defined as the laser pulse duration, τ_p . The maximum of the Gaussian pulse is shifted with respect to the start of the simulation (zero time) by $2.5\tau_p$ to ensure complete deposition of the laser pulse energy to the target. The attenuation of laser intensity with depth under the surface follows the Beer–Lambert law, and the optical penetration depth of 14.5 nm, taken based on the value of the absorption coefficient of pure Ni at a laser wavelength of 800 nm [77], is assumed in the simulations [64].

The dimensions of regions within the computational domain represented by different models are shown in the right panel of Fig. 1 and are chosen to ensure that all the essential processes are captured by the combined model. In particular, the depth of the initial target where the atomistic resolution of the TTM-MD model is required is defined by the maximum depth of melting in the simulation performed at the highest laser fluence. The chemical disorder of the single-phase solid solution FeNi alloy is responsible for a substantially lower thermal conductivity and stronger electron–phonon coupling as compared to pure Ni and Fe [64, 78], leading to a strong localization of the deposited laser energy and a shallow melting depth. As a result, a relatively small, as compared to earlier simulations performed for one-component metals [17, 18, 31–35], depth of 150 nm is found to be sufficient for the FeNi target. The initial thickness of the CG MD part of the liquid environment is chosen

to be 300 nm, which is sufficient for the representation of the interaction of the liquid with the ablation plume and the appearance of the cavitation bubble. The lateral dimensions of the TTM-MD and CG MD regions, 100 nm \times 100 nm, exceed the sizes of any structural or morphological features (NPs, subsurface voids, transient liquid structures) generated in the simulations of laser ablation. In particular, the lateral dimensions are more than 7 times larger than the diameter of the largest nanoparticle observed in all simulations. Overall, the MD part of the computational domain consists of 141 million metal atoms and 36 million CG particles.

The continuum-level descriptions of the heat transfer into the bulk of the metal target by the TTM equations and the shock wave propagation in the liquid environment by the one-dimensional HD model are computationally inexpensive, and the sizes of these parts of the model are chosen to be large enough to avoid any finite-size artifacts. The TTM region extends 1.05 μm below the atomistic TTM-MD region, which is sufficient to avoid any significant increase in the electron and lattice temperature at the bottom of the computational domain by the end of the simulation. The HD model represents 6 μm of water above the CG MD region with a one-dimensional mesh of 3000 cells, which is sufficient for tracking the propagation of a strong laser-induced shock wave for more than 3 ns.

3 Result and discussion

In this section, we first provide a detailed discussion of several representative large-scale simulations of PLAL selected to illustrate distinct ablation regimes, from the low-fluence regime where the maximum temperature does not exceed T_c , and only a small amount of the target material transforms into atomic clusters (Sects. 3.1 and 3.2), to the medium fluence regime, where large NPs form through roughening and decomposition of the dense metal layer accumulated at the interface with the liquid environment (Sects. 3.3 and 3.4), and to the high-fluence regime where some parts of the ablation plume remain in the supercritical state for nanoseconds and the NPs form at the phase decomposition front propagating from the interface with the liquid environment (Sect. 3.5). The conditions leading to the generation of NPs with a high density of crystal defects are considered in Sect. 3.6, and the fluence dependence of the NP yield and size distribution is discussed in Sect. 3.7. Finally, in Sect. 3.8, the results of individual simulations performed at fixed laser fluences are then mapped to a laser spot with a Gaussian spatial profile, where different ablation regimes and NP formation mechanisms are realized simultaneously in different parts of the laser spot. The resulting integral picture of PLAL occurring at the scale of the whole laser spot is represented in the form of spatially and time-resolved

maps of transient nonequilibrium states and channels of the NP formation predicted in the simulations.

3.1 Low fluence regime I: melting and subsurface voids

The lowest absorbed laser fluence considered in the large-scale atomistic simulations is 600 J/m^2 , which is more than twice as high as the threshold for surface melting of the NiFe target and about 20% above the photomechanical spallation (separation and ejection of a surface layer) threshold in vacuum [64]. Similar to the spallation in vacuum [53, 79, 80], the dynamic relaxation of laser-induced stresses creates conditions for the nucleation and growth of subsurface voids in the molten part of the target, which can be seen in the snapshots shown in Fig. 2 as early as 50 ps after the laser pulse. The generation of the high density of voids transforms the subsurface region into a transient “spongy” structure of interconnected liquid regions. The spongy structure coarsens due to the grows and coalesce of the voids during the following 100 ps, but then shrinks and completely disappears by 300 ps.

While the absorbed fluence applied in this simulation is above the spallation threshold in vacuum, the interaction of the expanding surface layer with the liquid environment slows down the upward motion of the surface, prevents the separation of the surface layer from the bulk of the target, pushes the surface layer back toward the target, and causes the collapse of the subsurface voids. Rapid vaporization of water in contact with the hot metal surface leads to the formation of a thin low-density vapor layer above the surface, as can be seen from the snapshots in Fig. 2.

The temperature of the surface of the irradiated target quickly decreases after the laser excitation, mainly due to the rapid electronic heat transfer to the bulk of the target. As a result, only 226 atoms (corresponds to about 0.14% of a (001) atomic layer on the surface of the target) evaporate

during the short time of the thermal spike at the surface. We can conclude, therefore, that the area within a laser spot where the absorbed fluence is lower than 600 J/m^2 does not contribute to the generation of NPs in PLAL.

3.2 Low fluence regime II: separation and redeposition of a surface layer

As the absorbed fluence increases to 800 J/m^2 , the peak temperature at the target surface reaches T_c by the time of $\sim 50 \text{ ps}$, when almost all energy of the laser pulse is deposited to the target, Fig. 3a. Heating of the material up to the critical temperature signifies the transition to the regime of “phase explosion,” [54–56] when a rapid (“explosive”) release of the vapor phase starts to contribute to the material decomposition and ejection [53, 81]. Only a shallow surface region undergoes the explosive phase decomposition at this fluence, though, and the dynamic relaxation of the laser-induced stresses still remains the dominant driving force responsible for the subsurface cavitation and the transient formation of spongy structure [79–81]. In contrast to the lower-fluence simulation discussed in Sect. 3.1, the growth of the subsurface voids leads to the transformation of the spongy structure to an array of liquid bridges connecting the hot metal layer formed at the interface with the liquid environment to the bulk of the target, as can be seen from the snapshots of atomic configurations shown in Fig. 4. Almost all of the bridges break up by 500 ps, but the layer is pushed back by the liquid environment and redeposits to the target by $\sim 650 \text{ ps}$.

The rapid drop of the average density of the spongy structure between 100 and 200 ps, Fig. 3b, and the eventual breakup of the liquid bridges interrupts the heat flow from the hot metal layer to the bulk of the target, allowing the target to solidify prior to the layer redeposition. The resolidification process can be followed in the density contour plot, Fig. 3b, where the difference in densities of the molten

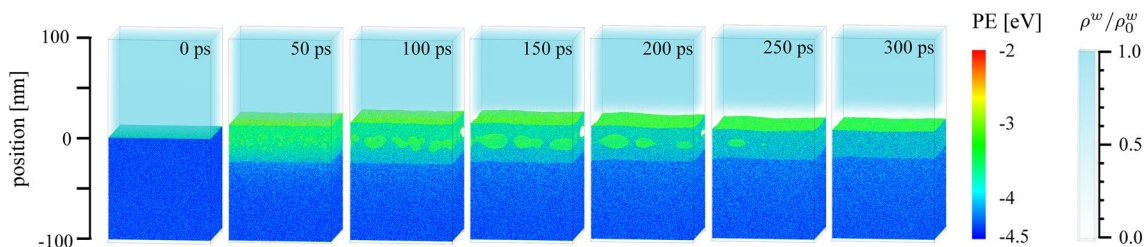


Fig. 2 Snapshots of atomic configurations obtained in a simulation of PLAL of a FeNi target irradiated by a 10 ps laser pulse at an absorbed fluence of 600 J/m^2 . Ni and Fe atoms are colored by their potential energy (PE), in the range of -4.5 to -2 eV . With this coloring scale, the crystalline part of the target is blue, the molten metal is light blue (reflecting the contribution of the latent heat of melting), the top surface and internal surfaces of voids are green, and vapor-

phase metal atoms are red. The shades of the light blue color above the target represent the local water density ρ^w normalized by the density of liquid water at 300 K, ρ_0^w , with the scale bar provided on the right. This color scheme is also used in snapshots shown in Figs. 4, 5a, 7, 12, and 17. Position zero is the initial position of the target-liquid interface. The lateral dimensions of the computational cell are $100 \text{ nm} \times 100 \text{ nm}$

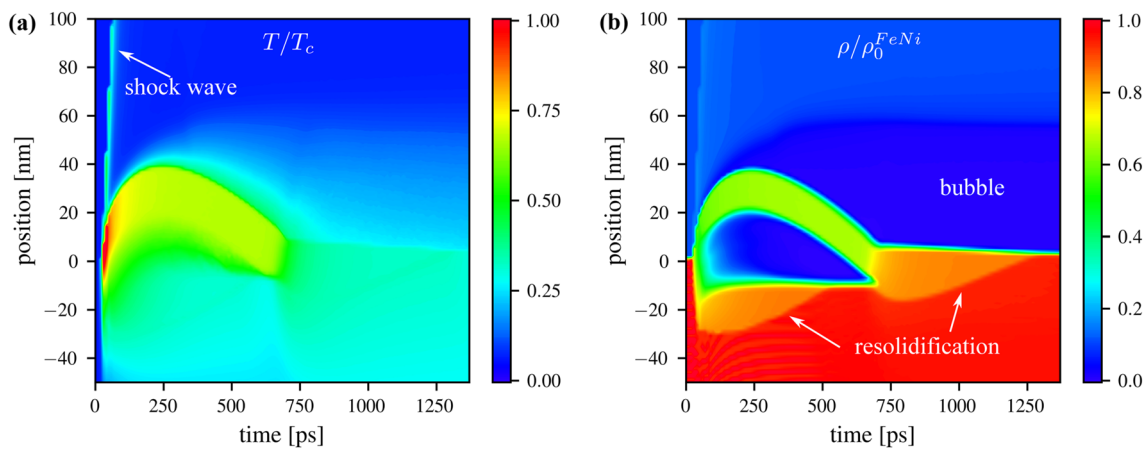


Fig. 3 Spatial and temporal evolution of temperature (a) and density (b) in a simulation of PLAL of a FeNi target irradiated by a 10 ps laser pulse at an absorbed fluence of 800 J/m^2 . The temperature is normalized by the thermodynamic critical temperature of FeNi, T_c , and the density is normalized by the density of FeNi crystal at 300 K, ρ_0^{FeNi} . The shock wave generated in the liquid environment by the ini-

tial expansion of the irradiated target and heating of the adjacent liquid is marked in (a). The solidification fronts in the FeNi target and the low-density vapor region above the target surface (“bubble”) are marked in (b). Position zero is the initial position of the target-liquid interface

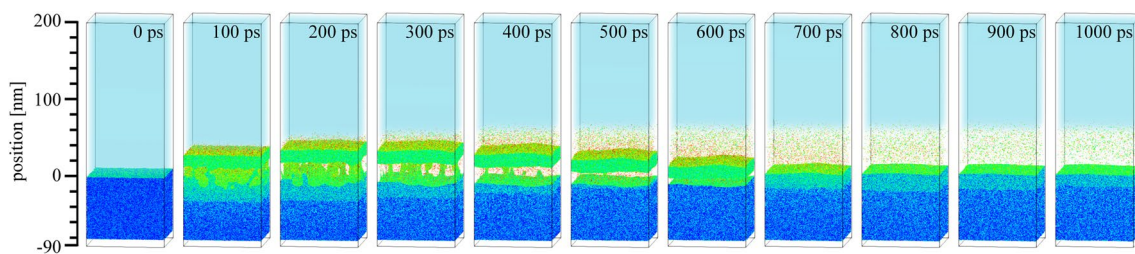


Fig. 4 Snapshots of atomic configurations obtained in a simulation of PLAL of a FeNi target irradiated by a 10 ps laser pulse at an absorbed fluence of 800 J/m^2 . The color scheme is the same as in Fig. 2. The atomic clusters and small NPs are generated through the condensation

of metal vapor in the low-density water-metal mixing region formed above the surface of the target. A spongy structure transiently appears below the molten layer at the early stage of the material expansion

and solid phases allows for identification of the solidification front, as well as from the snapshots in Fig. 4, where the contribution of the latent heat of melting to the potential energy of atoms is reflected in the colors of atoms in the molten and solid parts of the target. The redeposition of the hot metal layer at $\sim 650 \text{ ps}$ leads to a partial remelting of the surface region, which is followed by complete resolidification by 1.3 ns.

Similar to the simulation discussed in Sect. 3.1, the brief interaction of the liquid environment with the hot metal layer results in the vaporization of water and the formation of a low-density vapor layer above the surface of the target. The higher temperature of the metal layer and its slower cooling due to the transient separation from the target not only produces a larger vapor-phase region (denoted as “bubble” in Fig. 3b) but also results in more active evaporation of metal atoms into this region. The metal vapor rapidly cools down due to the interaction with colder water vapor and condenses

into small atomic clusters and NPs. In this paper, we identify the particles generated by PLAL through a cluster analysis [82] and describe the size of a particle in terms of the equivalent diameter D of a spherical crystalline particle with the same number of atoms N , i.e., $D = \sqrt[3]{3N/2\pi a}$, where a is the lattice parameters of a FeNi fcc crystal at 300 K.

An enlarged view of the vapor region provided in Fig. 5a for a time of 1 ns shows a substantial number of atomic clusters ($D < 1 \text{ nm}$, $N < 49$) and nanoparticles ($D \geq 1 \text{ nm}$, $N \geq 49$) formed through the evaporation–condensation process. Most of the particles in this region are clusters with D ranging from 0.5 to 1 nm, and the mass fraction of NPs is only 13%, as can be seen from the particle size distribution shown in the form of a pie chart in Fig. 5b. The variation of the total amount of material converted to the atomic clusters and NPs with time is shown in Fig. 5c, where the particle yield is expressed in terms of the equivalent ablation depth, i.e., the thickness of a surface layer of the initial target containing the

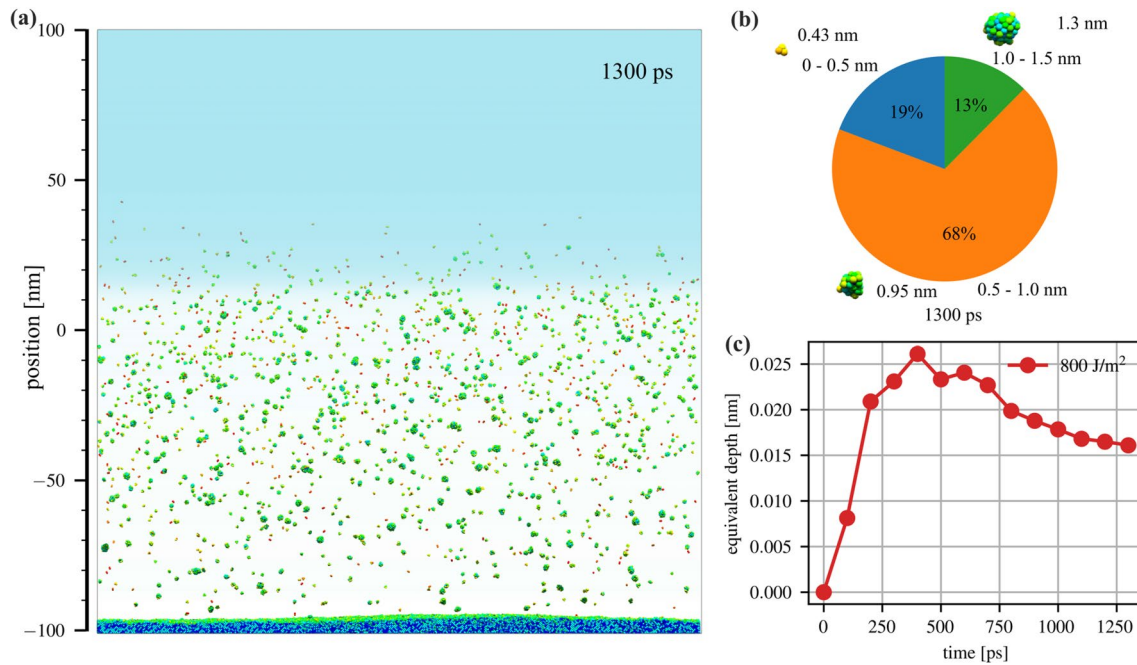


Fig. 5 An enlarged view of a low-density vapor region formed above the irradiated surface **(a)**, a mass-weighted pie chart size distribution of nanoparticles/clusters at 1 ns **(b)**, and the time dependence of the equivalent depth of the target material converted to clusters and NPs **(c)** predicted in a simulation of PLAL at an absorbed fluence of 800 J/m^2 . The snapshot in **(a)** corresponds to the last panel of Fig. 4. Note that the depth of the computational system in the view direction is 100 nm, and all clusters and NPs present in the system are projected

on the view plane in the snapshot. In **(b)**, the size of a NP or a cluster is characterized by the equivalent diameter D of a spherical particle with the same number of atoms, as described in the text. The atomic configurations of three particles shown in **(b)** are representative of the three size groups distinguished in the pie chart. In **(c)**, the amount of material converted to atomic clusters and NPs is expressed in terms of the equivalent depth, defined as the thickness of a surface layer of the initial target that contains the same number of atoms

same number of atoms. The initial increase of the equivalent depth is due to the rapid evaporation from the hot metal surface and condensation of the metal vapor into atomic clusters and NPs. The steady decrease after 600 ps is due to the redeposition of clusters and NPs to the rapidly cooled surface of the target.

The ablation yield at this fluence is still very low and corresponds to $\sim 9.2\%$ of a single (001) atomic layer. Nevertheless, we consider the absorbed fluence of 800 J/m^2 to be the threshold fluence for the onset of NP formation in PLAL of the FeNi target. This assessment is supported by the fluence dependence of the NP yield at higher fluences discussed below (e.g., see Fig. 25b in Sect. 3.7).

3.3 Medium fluence regime I: roughening and decomposition of interfacial layer

As the absorbed laser fluence increases, so does the temperature of the metal layer accumulated at the interface with the liquid environment. At $F_{\text{abs}} = 1350 \text{ J/m}^2$, the temperature of the interfacial layer exceeds the critical temperature of FeNi at the initial stage of the ablation plume accumulation and the interfacial layer formation. This is illustrated in Fig. 6a, where the T_c isotherm is

shown by the dashed line. The interaction of the hot metal layer with the liquid environment and the expansion of the layer following its initial accumulation at the plume-liquid interface leads to the cooling of the layer. By the time the interfacial layer reaches its highest position, the temperature of the layer drops below T_c . Similar to the lower fluence simulations discussed in Sects. 3.1 and 3.2, the dense metal layer is pushed back by the liquid environment and redeposits to the target by 750 ps, Fig. 6b. Despite the high temperature of the top part of the ablation plume, the lower part remains colder, and the interfacial layer remains connected to the bulk of the target by a colder spongy structure of interconnected liquid regions generated by the unloading of the laser-induced compressive stresses. The spongy structure coarsens with time and finally collapses upon the redeposition of the metal layer reflected from the interface with the liquid environment. Similar to the simulation discussed in Sect. 3.2, the redeposition of the hot metal layer reheats the target and temporarily reverses the direction of the liquid-crystal interface propagation, from the slow upward motion (solidification) between 200 and 750 ps to the downward motion (melting) after 750 ps. The dynamics of the crystallization/melting front can also be seen from the snapshots shown in Fig. 7.

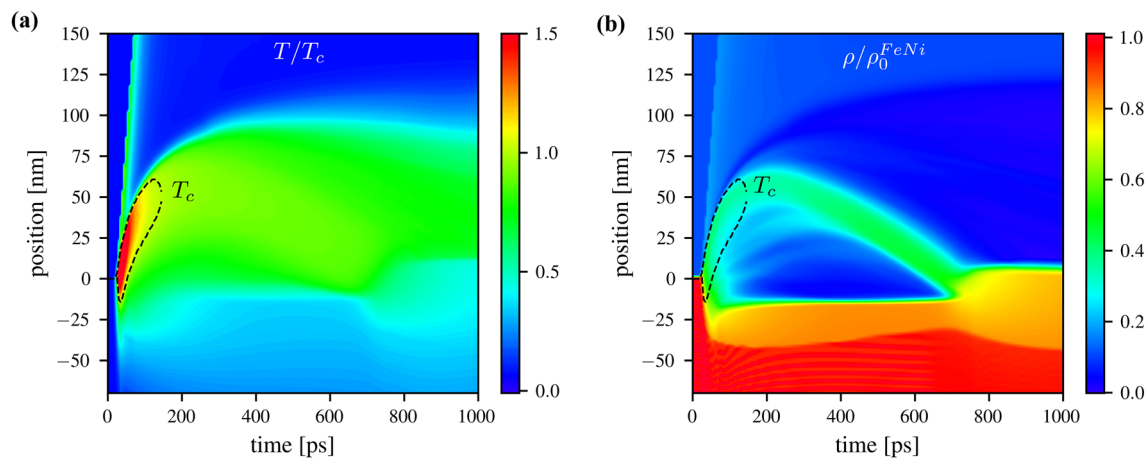


Fig. 6 Spatial and temporal evolution of temperature **(a)** and density **(b)** in a simulation of PLAL of a FeNi target irradiated by a 10 ps laser pulse at an absorbed fluence of 1350 J/m^2 . The temperature is normalized by the thermodynamic critical temperature of FeNi, T_c ,

and the density is normalized by the density of FeNi crystal at 300 K, ρ_0^{FeNi} . The dashed lines outline the region where the temperature is higher than T_c . Position zero is the initial position of the target-liquid interface

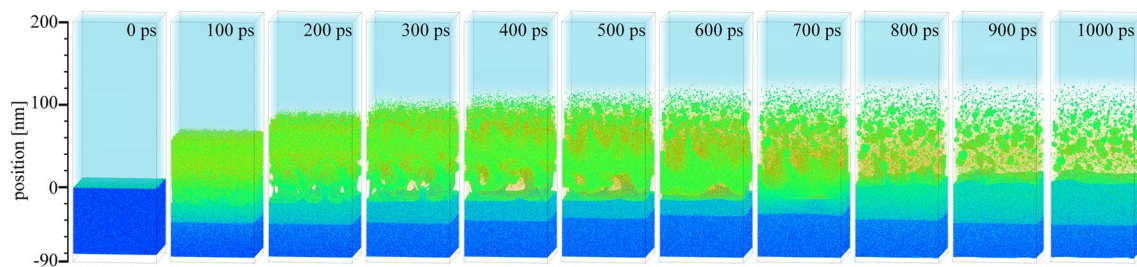


Fig. 7 Snapshots of atomic configurations obtained in a simulation of PLAL of a FeNi target irradiated by a 10 ps laser pulse at an absorbed fluence of 1350 J/m^2 . The color scheme is the same as in Fig. 2. Two channels of the NP generation can be identified: (1) condensa-

tion of metal vapor in the low-density water-metal mixing region and (2) roughening and decomposition of the top part of the dense metal layer accumulated at the plume-liquid interface

In contrast to the lower-fluence simulations illustrated by Figs. 2 and 4, where the upper surface of the metal layer generated at the interface with the liquid environment remains flat until its redeposition to the target, the higher temperature of the interfacial layer in the simulation performed at $F_{\text{abs}} = 1350 \text{ J/m}^2$ makes it unstable against nanoscale roughening and decomposition into NPs, Fig. 7. The roughening and decomposition of the top part of the interfacial layer can be attributed to the Rayleigh–Taylor instability emerging due to the rapid deceleration of the higher density metal layer by the pressure exerted from the much lighter liquid environment, Fig. 6b, as discussed for earlier simulations performed for Ag bulk targets [17, 18, 32] and thin films [31, 35]. The high values of the deceleration of the interface, the large difference in densities between the metal layer and liquid environment, and the low value of the interfacial tension at temperatures close to T_c of the metal are reducing the time- and length-scales of the interface roughening and decomposition into NPs [18] down to $\sim 100 \text{ ps}$ and $\sim 10 \text{ nm}$, Fig. 7.

The formation of NP through the roughening and decomposition of the top part of the transient interfacial layer is visualized in Fig. 8, where the atoms in the snapshots are colored according to the size of the particles they belong to. In addition to the numerous atomic clusters and small NPs forming in the low-density plume-liquid mixing region through the evaporation–condensation mechanism and colored blue, first larger NPs are also observed to emerge from the interface roughening and decomposition as early as 400 ps. More NPs with sizes ranging from 4 to 12 nm form through this mechanism between 400 and 800 ps, as the hot metal layer moves down and redeposits to the target. The formation of these larger NPs cannot be attributed to a gradual growth through the condensation or coalescence of smaller clusters and NPs. Rather, they form through a distinct mechanism related to the nanoscale hydrodynamic instability of the rapidly decelerated plume-liquid interface. As discussed above, this mechanism of NP formation is similar to that revealed in earlier

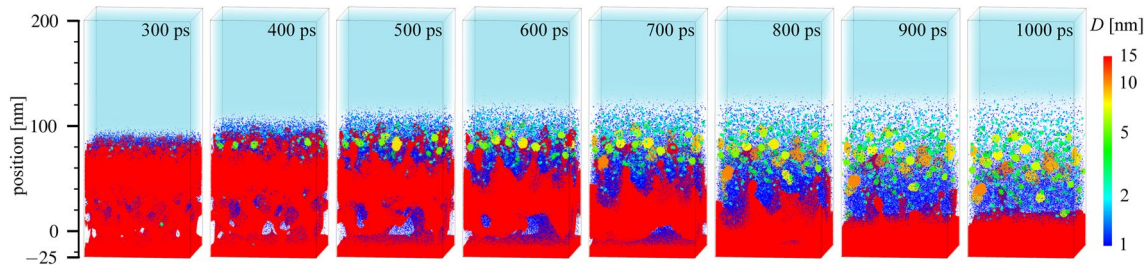


Fig. 8 Snapshots from a simulation illustrated in Fig. 7, with atoms colored by size (equivalent diameter D) of the cluster or NP they belong to. The NPs are identified by cluster analysis [82], and the molten regions connected to the bulk of the target constitute a single entity colored red

simulations of Ag targets [17, 18, 32], even though the heat-affected zone in Ag is substantially larger due to the higher thermal conductivity and weaker electron–phonon coupling. The larger depth affected by the laser heating in a Ag target leads to the ejection of more material, formation of a thicker interfacial layer, slower emergence of larger-scale interfacial roughness, and generation of larger NPs that can be driven into the liquid environment by a sequence of hydrodynamic instabilities at the plume–liquid interface [17, 18]. Compared with the PLAL simulations of Ag, the FeNi NPs produced through this mechanism are smaller, more numerous, and remain within the emerging cavitation bubble.

The coexistence of two distinct mechanisms of NP formation can be clearly seen from the evolution of the distribution of NPs of different sizes above the irradiated target surface, Fig. 9. By 200 ps, the ablation plume has already accumulated at the interface with the liquid environment (Fig. 6b), a low-density vapor region has appeared above the interfacial layer, and a spongy structure of interconnected liquid regions has been formed below the interfacial layer. The atomic clusters and small NPs with sizes below 3 nm, formed through the evaporation–condensation mechanism, are present both above and below the interfacial layer, i.e., in the low-density metal–liquid mixing region above the interfacial layer and in the empty space within the spongy structure. Compared to the particles formed through the same mechanism at $F_{\text{abs}} = 800 \text{ J/m}^2$, where $D < 1.5 \text{ nm}$ in Fig. 5b, the maximum size of the NPs is larger, which is related to the higher temperature and more intense evaporation of the interfacial layer. As time progresses, the molten layer redeposits, the spongy liquid structure collapses, and the small particles formed within this structure (region to the left from the red arrows in Fig. 9a, b) are erased. The atomic clusters and NPs in the region above the molten layer (or above the new surface of the target after the layer redeposition at 750 ps) gradually coarsen to the maximum size of $\sim 4 \text{ nm}$ and spread along a broad region between the target surface and the outer boundary of the slowly expanding low-density vapor region (located at $\sim 130 \text{ nm}$ at 1 ns).

The nanodroplets generated by the second mechanism of the NP formation, through the roughening and decomposition of the top part of the interfacial metal layer, have larger sizes ($D > 4 \text{ nm}$) and appear as a distinct group in the distributions shown in Fig. 9b–d. Since these NPs form at the upper interface of the metal layer, they initially appear within a narrow region (60 to 90 nm at 500 ps) and then spread downwards as the metal layer moves toward the target.

By 750 ps, the molten layer redeposits to the target surface and starts to cool down rapidly due to the heat transfer to the bulk of the target (Fig. 6a). As a result, both channels of the generation of new NPs, through the evaporation–condensation and the decomposition of molten structures, shut down shortly after the metal layer redeposition. Indeed, the spatial and size distributions shown in Fig. 9c, d for 800 ps and 1 ns are rather similar. The only notable difference between these two distributions is the decrease in the numbers of small clusters, which join larger NPs and redeposit to the surface of the target.

The analysis of the spatial distribution of NPs of different sizes can be further illustrated by more conventional mass-weighted size distributions shown for 200, 500, 600, and 800 ps in Fig. 10. By 200 ps, only atomic clusters and NPs with $D < 4 \text{ nm}$ form through the evaporation–condensation mechanism. The total mass of the particles in this range increases until 500 ps, stays at an approximately constant level until 600 ps, and then decreases due to the redeposition to the target surface and coalescence into larger NPs. At the same time, a distinct population of larger NPs with D ranging from 4 to 10 nm appears in the distribution shown for 500 ps, which is consistent with the snapshot shown for 500 ps in Fig. 8 and the corresponding distribution in Fig. 9b. This population, attributed to the roughening and decomposition of the top part of the interfacial metal layer, continues to grow until the redeposition of the metal layer to the target at about 750 ps. By this time, the total mass of the small particles ($D < 4 \text{ nm}$) formed through the evaporation–condensation mechanism and the larger ones ($D > 4 \text{ nm}$) formed through the interface roughening and

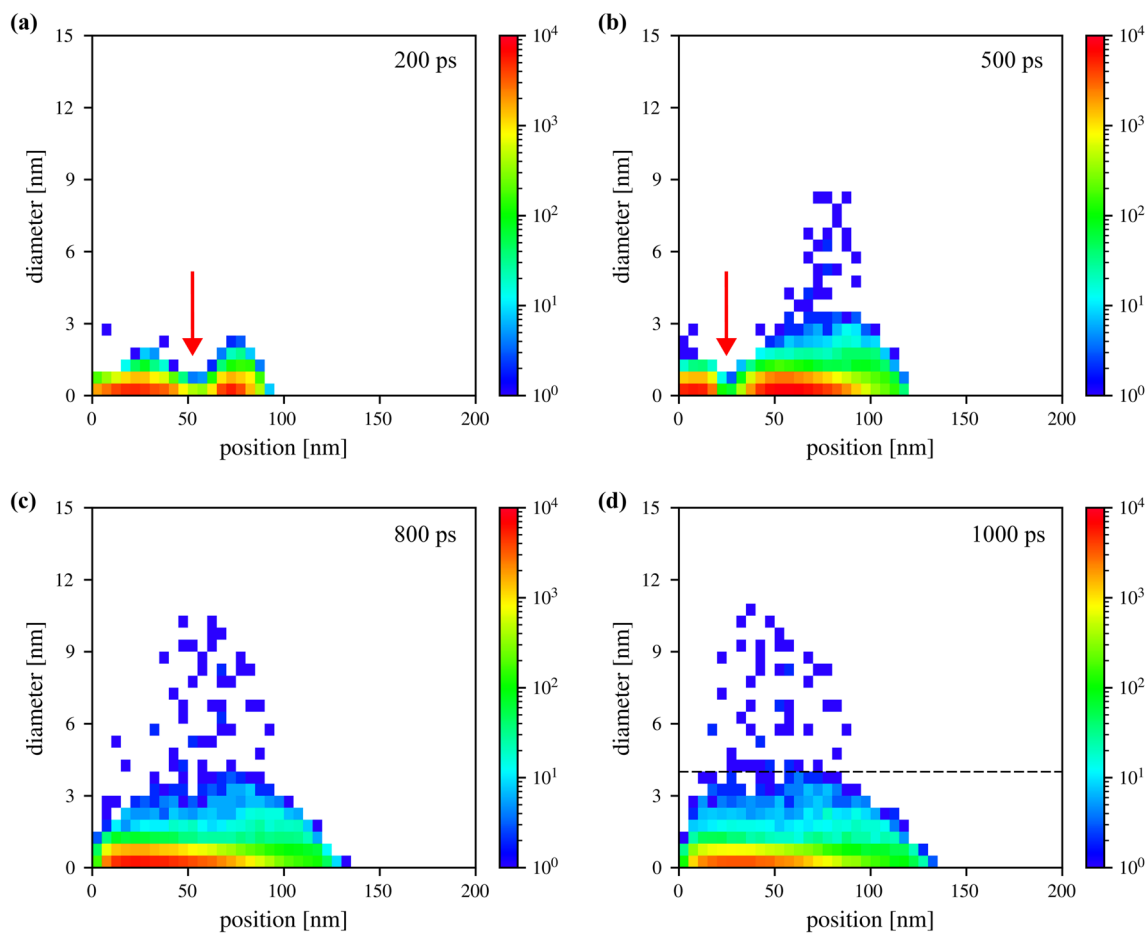


Fig. 9 Distributions of NPs of different sizes in the ablation plume calculated for 200, 500, 800, and 1000 ps in the simulation performed at $F_{\text{abs}} = 1350 \text{ J/m}^2$. The parameter space is discretized into bins (pixels) with a horizontal size of 5 nm for the positions above the initial target-liquid interface and a vertical size of 0.5 nm for the equivalent diameters D of the clusters or NPs. Each rectangular pixel is colored by the number of clusters or NP in the corresponding bin. The dark blue color corresponds to one particle in a bin. The same

decomposition are approximately equal, suggesting that the two mechanisms make comparable contributions to the NP generation at this absorbed fluence.

3.4 Medium fluence regime II: layered structure of the ablation plume

An increase in absorbed fluence by only 11%, from 1350 to 1500 J/m^2 , results in substantial qualitative changes in the ablation dynamics and nanoparticle formation mechanisms. These changes are indicative of an abrupt threshold-like transition between the ablation regimes and call for a close examination of the results of this simulation. The difference between the two simulations is apparent from the comparison of the density contour plots shown in Figs. 6b and 11b. In contrast to the simulation performed at $F_{\text{abs}} = 1350 \text{ J/m}^2$,

representation of the size distributions is used in Figs. 14 and 20. The red arrows in (a, b) mark the approximate location of the center of the molten metal layer. The horizontal dashed line in (d) separates the parts of the distribution where two different NP formation mechanisms make dominant contributions: condensation of atoms evaporated from the hot interfacial metal layer for $D < 4 \text{ nm}$ and decomposition of a rough interface of the metal layer for $D > 4 \text{ nm}$

where the ablation plume accumulates in a single interfacial layer connected to the target by liquid bridges, at $F_{\text{abs}} = 1500 \text{ J/m}^2$ the formation of two distinct high-density regions is observed.

In the upper part of the ablation plume, hot material that originates from the top surface region of the target heated up to a maximum temperature of $1.5T_c$ accumulates and remains in the supercritical state until about 250 ps. The temperature of this layer then drops below T_c as it expands in both directions, pushing the liquid further away from the target and driving some of the ejected material down toward the target surface. The expansion and rapid cooling make the single-phase supercritical fluid unstable with respect to the spinodal phase separation into two stable phases, liquid, and vapor [54, 83]. Since the density of the top part of the ablation plume is much closer to the density of vapor than that of

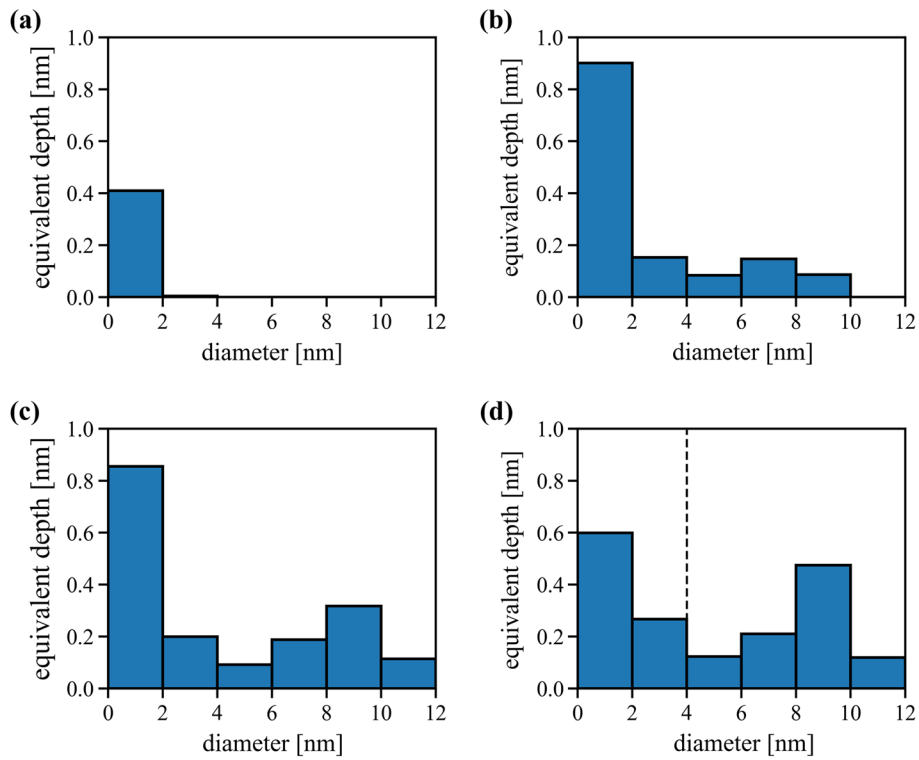


Fig. 10 Mass-weighted size distributions of atomic clusters and NPs predicted in a simulation performed at $F_{\text{abs}} = 1350 \text{ J/m}^2$ for times of 200, 500, 600, and 800 ps. The size of a NP or a cluster is characterized by the equivalent diameter D of a spherical particle consisting of the same number of atoms. The amount of target material converted to clusters and/or NPs within the size range of each bin is expressed in terms of the equivalent depth of a surface layer of the initial target that contains the same number of atoms. The individual metal atoms

are included in the first bin of the histograms. The summation over all bins gives the total ablation yield (expressed in terms of the ablation depth) at a given moment of time. The vertical dashed line in (d) separates the parts of the distribution where two different NP formation mechanisms make dominant contributions: condensation of atoms evaporated from the hot interfacial metal layer for particles with diameter $D < 4 \text{ nm}$ and decomposition of a rough interface of the metal layer for larger NP with $D > 4 \text{ nm}$

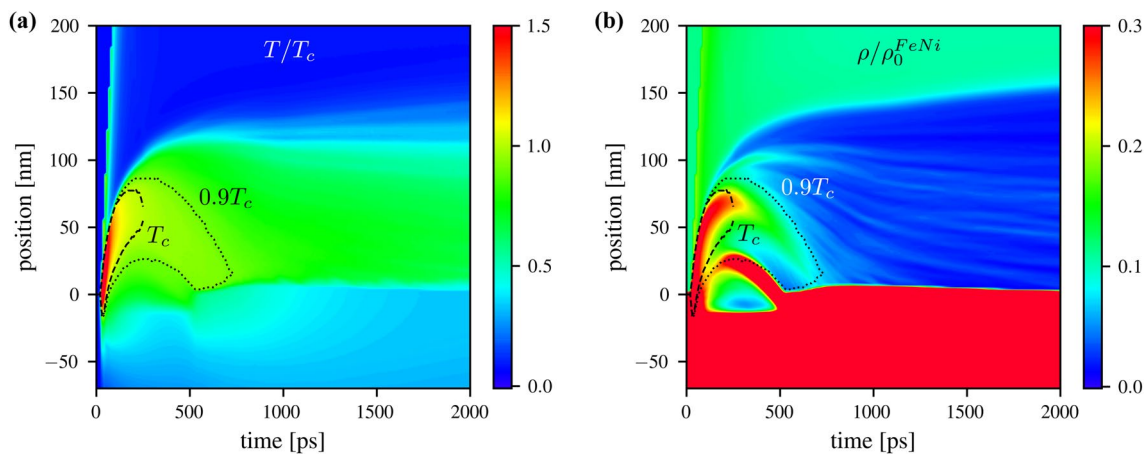


Fig. 11 Spatial and temporal evolution of temperature (a) and density (b) in a simulation of PLAL of a FeNi target irradiated by a 10 ps laser pulse at an absorbed fluence of 1500 J/m^2 . The temperature is normalized by the thermodynamic critical temperature of FeNi, T_c ,

and the density is normalized by the density of FeNi crystal at 300 K, ρ_0^{FeNi} . The dashed and dotted lines are T_c and $0.9T_c$ isotherms, respectively. Position zero is the initial position of the target-liquid interface

the liquid phase, the decomposition of the supercritical fluid produces a mixture of nanodroplets and vapor, as can be seen from the density variation in Fig. 11b, as well as from the snapshots shown in Fig. 12. The density of vapor produced by the phase decomposition is decreasing with time, as the vapor condenses on the NPs and the rapidly cooled surface of the target. This can be seen from the snapshots in Fig. 12, where the vapor phase atoms have higher potential energy and appear as red dots.

In the lower part of the ablation plume, the temperature rapidly drops below T_c , the density is higher, and the expanding material decomposes into a spongy structure of interconnected liquid regions, similar to that observed at

$F_{\text{abs}} = 1350 \text{ J/m}^2$. In contrast to the lower-fluence simulation, the spongy structure does not extend all the way to the top interfacial layer (Fig. 8) but is localized near the surface of the target and collapses shortly after 500 ps. The collapse is driven by pressure exerted on the top layer of the spongy structure by the expanding upper region of the plume undergoing the phase separation from the supercritical state.

The mass transfer and material conversion to NPs are further illustrated in Fig. 13 by the density profiles plotted for the liquid environment (blue) and metal (magenta), as well as in Fig. 14 by the spatial distribution of NPs of different sizes. Three density peaks that appear at the initial dynamic stage of the ablation process are marked in these

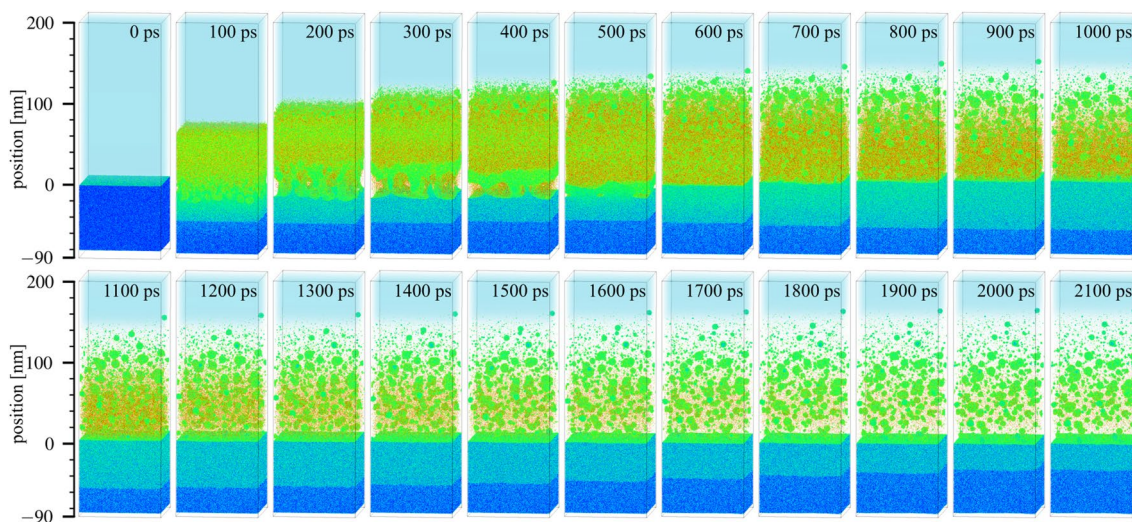


Fig. 12 Snapshots of atomic configurations obtained in a simulation of PLAL of a FeNi target irradiated by a 10 ps laser pulse at an absorbed fluence of 1500 J/m^2 . The color scheme is the same as in Fig. 2. The formation of a transient spongy structure of intercon-

nected liquid regions can be seen between 100 and 400 ps, while the phase separation from the supercritical state produces the nanodroplets and vapor in the upper part of the plume

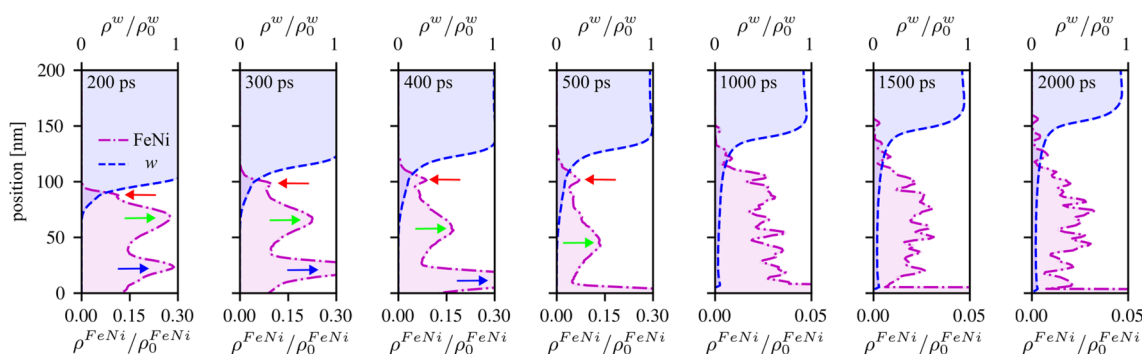


Fig. 13 The density profiles calculated for the FeNi plume (dot-dashed magenta lines) and water (dashed blue lines) in a simulation of PLAL of a FeNi target irradiated by a 10 ps laser pulse at an absorbed fluence of 1500 J/m^2 . The density of the FeNi plume is normalized by the density of FeNi crystal at 300 K, ρ_0^{FeNi} , and the density of water is normalized by the room temperature water den-

sity, ρ_0^w . The red, green, and blue arrows mark the density peaks that correspond to the location of the NP formation at the plume–water interface, the hot homogeneous (supercritical and close-to-critical) layer of the ablation plume, and the molten layer covering the spongy structure of liquid regions connected to the target, respectively

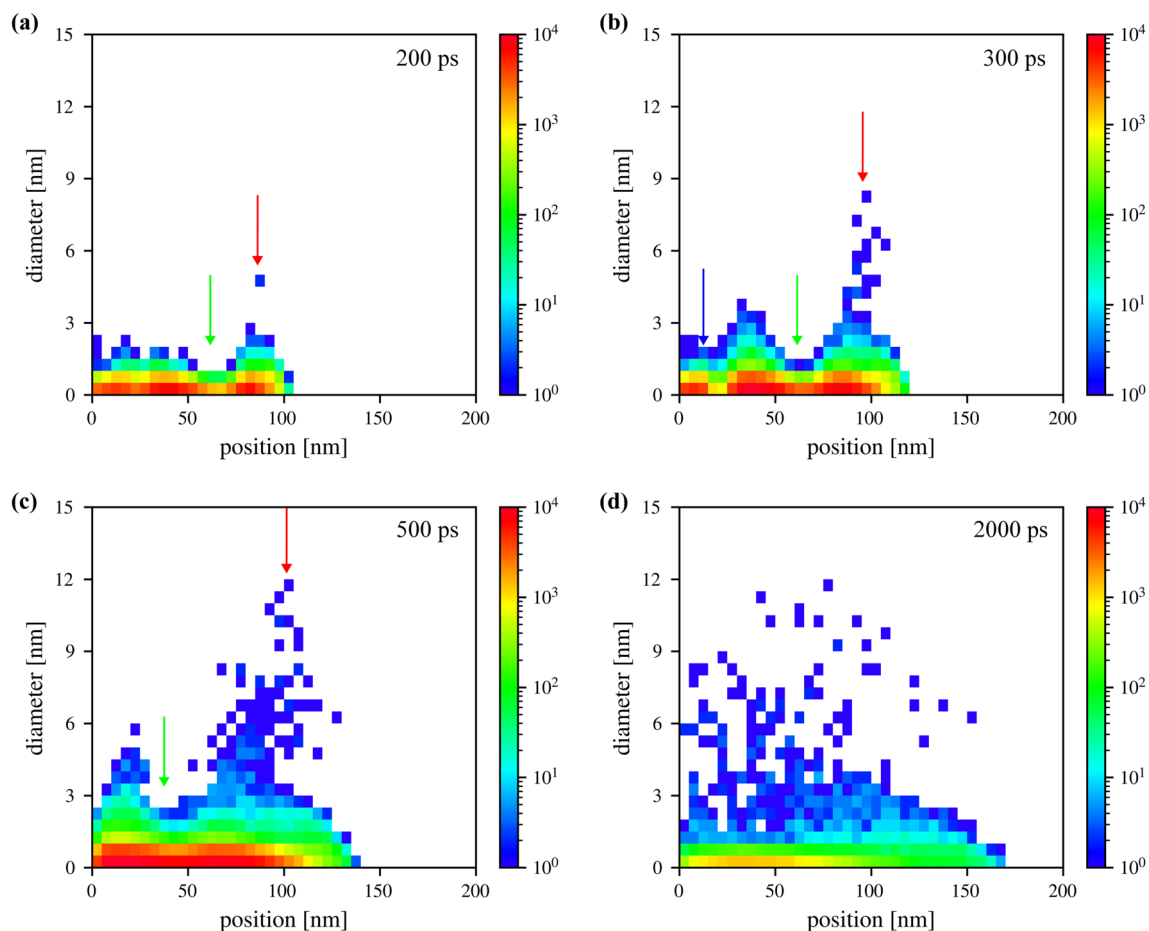


Fig. 14 Distributions of NPs of different sizes in the ablation plume calculated for 200, 300, 500, and 2000 ps in the simulation performed at $F_{\text{abs}} = 1500 \text{ J/m}^2$. The rectangular pixels are colored based on the number of clusters or NPs at locations and within the particle size ranges defined by the x - and y -axes, as explained in the caption of

Fig. 9. Similar to Fig. 13, the red, green, and blue arrows mark the locations of the NP formation at the plume–water interface, the hot homogeneous (supercritical and close-to-critical) layer of the ablation plume, and the molten layer covering the spongy structure of liquid regions connected to the target, respectively

figures by arrows. The red arrow shows the location where the hot supercritical plume gets in contact with the cold liquid environment. The mixing with liquid results in a rapid cooling of the plume and formation of first NPs. The NPs can already be observed at 200 ps, when the largest one has an equivalent diameter of about 5 nm, Fig. 14a. The maximum size of the NPs in this region grows with time and reaches 12 nm by 500 ps, Fig. 14c.

The second broader density peak marked by the green arrow corresponds to the location of the hot metal layer accumulated close to the interface with the liquid environment and reflected back toward the target. The metal plume in this layer is initially in the supercritical state but cools down below T_c by about 250 ps. The upper part of this layer decomposes into vapor and nanodroplets, but the lower part stays above $0.9T_c$ (Fig. 11a) and remains largely homogeneous (Fig. 11b) until its redeposition to the target at about 700 ps.

The blue arrow shows the location of the interface between the spongy liquid structure connected to the target and the hot homogeneous plume above. The heat transfer to the bulk of the target cools down the spongy structure, leading to the formation and growth of a continuous liquid layer on top of the spongy structure through the condensation of the material above this layer. The formation and growth of the continuous liquid layer can be seen in the snapshots shown for 300 and 400 ps in Fig. 12, while the density drop above this layer due to the condensation can be seen in Figs. 11b and 13. After the redeposition of the molten layer topping the spongy structure (blue arrows in Figs. 13 and 14) at around 500 ps and the hot cloud of the close-to-critical plume (green arrows in Figs. 13 and 14) at about 700 ps, the NPs spread evenly throughout the slowly expanding cavitation bubble, as can be seen from the distribution shown for 2 ns in Fig. 14. The water vapor reaches the surface of the target by 1 ns

and equilibrates with the metal plume (see water density profile in Fig. 13). The gradual decrease in density of the plume between 1 and 2 ns (Fig. 13) is related to the condensation of vapor and redeposition of NPs and clusters to the target surface undergoing rapid cooling by the heat transfer to the bulk of the target. The density drop due to the condensation/redeposition is particularly pronounced within the 50-nm-wide region adjacent to the target surface.

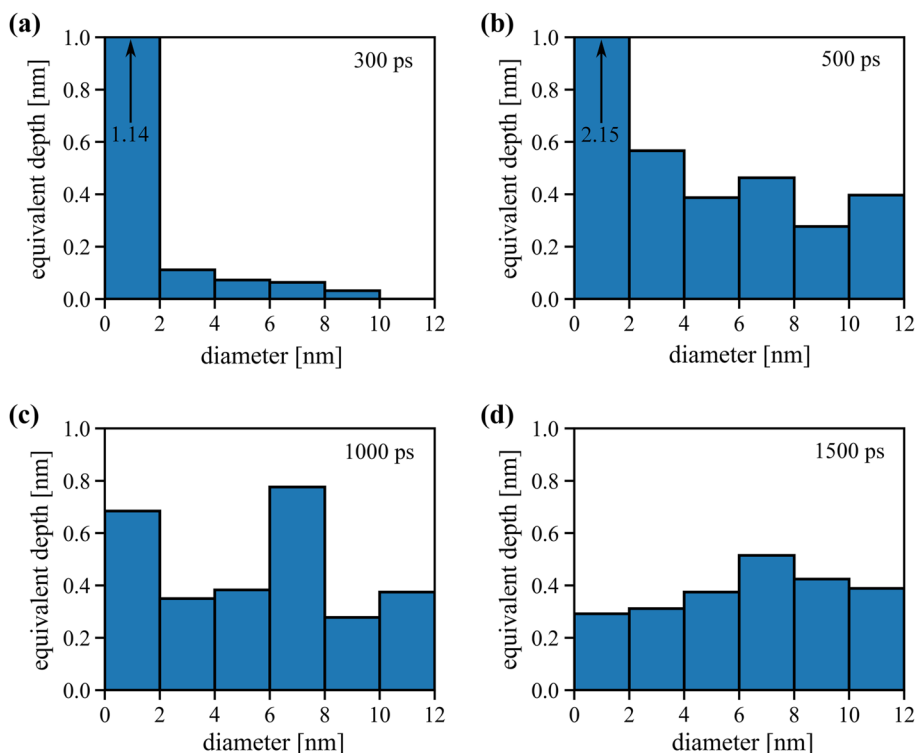
The processes contributing to the NP formation described above are reflected in the evolution of the mass-weighted NP size distributions shown in Fig. 15. The atomic clusters and small nanoparticles ($D < 2$ nm), generated mainly by the phase decomposition of the supercritical fluid, dominate the size distribution at 300 ps, although first larger NPs also appear at this time at the plume-liquid interface. The phase decomposition of the rapidly expanding upper part of the ablation plume produces more large droplets, atomic clusters, and vapor between 300 and 500 ps. After that, the number of atomic clusters and NPs with $D < 8$ nm starts to decrease, while the total mass of large NP with $D > 8$ nm increases. This increase, however, does not balance the decrease in the mass of the smaller particles, reflecting the redeposition of the ablation plume to the target. Since the largest NPs tend to form further away from the target (Fig. 14), the population of these NPs is less affected by the redeposition.

3.5 High fluence regime: phase separation from the supercritical state

The increase of the laser fluence above the threshold level of 1500 J/m^2 leads to the generation of a supercritical plume that spreads throughout the emerging cavitation bubble at the initial stage of the plume expansion. The pressure exerted by the supercritical fluid fully suppresses the formation of the spongy liquid structure near the surface of the target, and the NP generation occurs mainly through the propagation of a phase separation front into the plume cooled from the supercritical state. This ablation regime is illustrated in this section by a simulation performed with an absorbed fluence of 3000 J/m^2 .

Based on the contour plots shown in Fig. 16 and the snapshots shown in Fig. 17, three stages of the ablation dynamics can be distinguished. At the first stage, the surface region of the target is heated to a maximum temperature of $4T_c$ by the laser pulse and expands rapidly against the liquid environment, pushing it up by 200 nm in just 250 ps. The temperature of the plume decreases below $2T_c$ during this initial expansion, but most of the plume still remains in the supercritical state (Fig. 16a). The interface between the ablation plume and the liquid environment stays rather sharp during the initial rapid expansion, as can be seen from the snapshots shown in Fig. 17 for 100 and 200 ps.

Fig. 15 Mass-weighted size distributions of atomic clusters and NPs predicted in a simulation performed at $F_{\text{abs}} = 1500 \text{ J/m}^2$ for times of 300, 500, 1000, and 1500 ps. The size of a NP or a cluster is characterized by the equivalent diameter D of a spherical particle consisting of the same number of atoms. The amount of target material converted to clusters and/or NPs within the size range of each bin is expressed in terms of the equivalent depth of a surface layer of the initial target that contains the same number of atoms. The individual metal atoms are included in the first bin of the histograms. The summation over all bins gives the total ablation yield (expressed in terms of the ablation depth) at a given moment of time



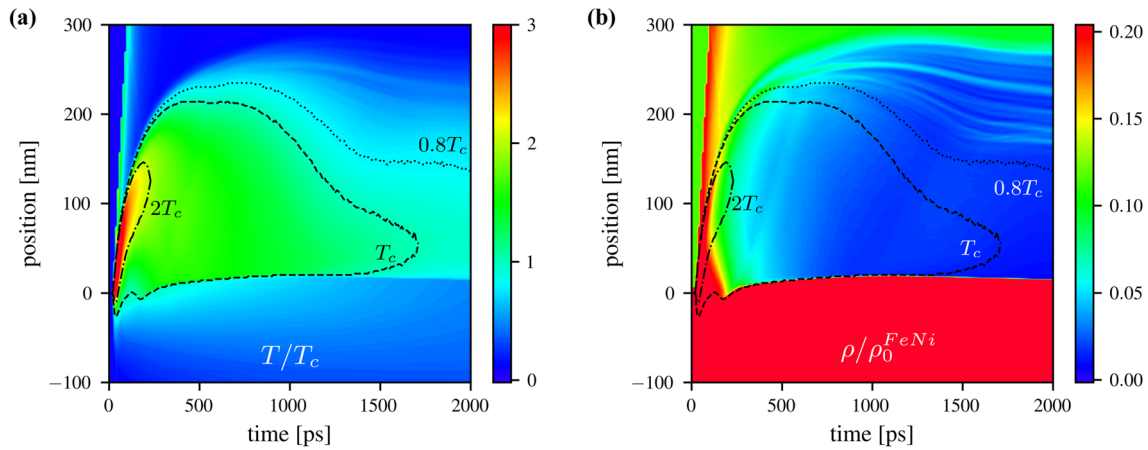


Fig. 16 Spatial and temporal evolution of temperature (a) and density (b) in a simulation of PLAL of a FeNi target irradiated by a 10 ps laser pulse at an absorbed fluence of 3000 J/m^2 . The temperature is normalized by the thermodynamic critical temperature of FeNi, T_c ,

and the density is normalized by the density of FeNi crystal at 300 K, ρ_0^{FeNi} . The dot-dashed, dashed and dotted lines are $2T_c$, T_c , and $0.8T_c$ isotherms, respectively. Position zero is the initial position of the target-liquid interface

The interfacial region starts to gradually broaden during the second stage of the ablation process, which lasts between 200 and 800 ps. During this time, the top part of the plume cools down due to the interaction with the liquid environment and decomposes into droplets, atomic clusters, and vapor. As can be seen from Fig. 16, the decomposition front roughly follows the isotherm of $0.8T_c$, which remains relatively stagnant until about 800 ps. During this time, the Brownian motion of NPs formed within an initially compact interfacial layer spreads out the NPs over a broader region (Fig. 17) and allows for easier access of water to deeper parts of the ablation plume.

Mixing with water cools the deeper regions of the ablation plume and drives the propagation of the front of the phase decomposition from the plume-liquid interface toward the surface of the target. The cooling becomes less effective as the water vapor diffuses further away from the cold outer surface of the cavitation bubble, as can be seen from the flattening of $0.8T_c$ isotherm in Fig. 16a and stagnation of the phase decomposition front after about 1.4 ns, apparent from the snapshots in Fig. 17. Interestingly, despite the rapid cooling of the target surface, the ablation plume in the immediate vicinity of the surface remains in the supercritical or close-to-critical homogeneous state until the end of the simulation at 2.1 ns. It is reasonable to expect that further propagation of the phase decomposition front toward the surface will convert the remaining homogeneous part of the ablation plume into NPs within a few more nanoseconds.

The mass transport and the material conversion to NPs during the three stages of the ablation process discussed above are further illustrated by the density profiles shown

in Fig. 18. At the end of stage 1, *i.e.*, at 200 ps, the plume-liquid interface remains relatively sharp and plume density variation reflects the temperature gradient within the supercritical plume (density is higher in the colder part of the plume adjacent to the target, Fig. 16a). By 500 ps, the plume density drops by more than a factor of two due to the redeposition to the target and further expansion against the liquid environment, the density profile equalizes, and the plume-liquid interface broadens. The broadening of the interface at this second stage of the ablation process is related to the cooling of the dense metal layer formed at the plume-liquid interface (marked by black arrows in Fig. 18) below $0.8T_c$ and the decomposition of this layer into individual NPs.

An enlarged view of the interfacial layer decomposition is provided in Fig. 19, where the NPs are colored by their sizes. A thin layer of NPs, with some of them larger than 5 nm, has already formed at the plume-liquid interface by 400 ps. This layer broadens with time, as the NPs move apart from each other through the Brownian motion. The NPs moving toward the liquid environment experience the highest cooling rate and solidify on a timescale of nanoseconds (see Sect. 3.6), while the NPs moving toward the target grow by consuming vapor and small clusters produced by the phase decomposition of the lower part of the plume.

The broadening of the initially compact interfacial layer is reflected in a splitting of the single interfacial peak in the density profiles shown in Fig. 18 for 200 and 500 ps into multiple peaks at later times. The spreading of the nanoparticles makes it easier for the liquid to mix with the ablation plume and cool it down to the temperature required for the onset of the rapid phase decomposition, $0.8T_c$. The red

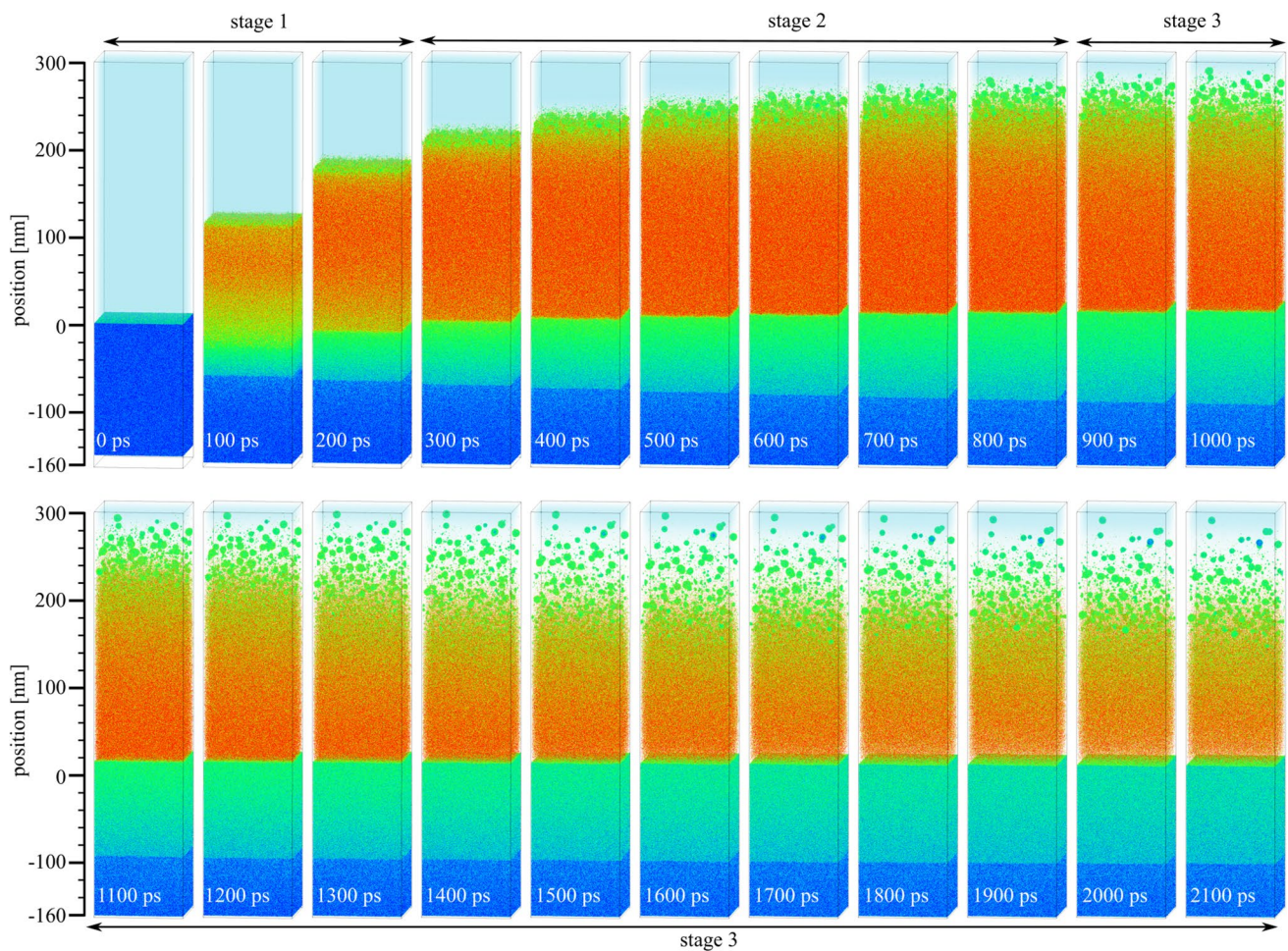


Fig. 17 Snapshots of atomic configurations obtained in a simulation of PLAL of a FeNi target irradiated by a 10 ps laser pulse at an absorbed fluence of 3000 J/m². The color scheme is the same as in

Fig. 2. The time spans of the three stages of the ablation process discussed in the text are marked by the double-headed arrows

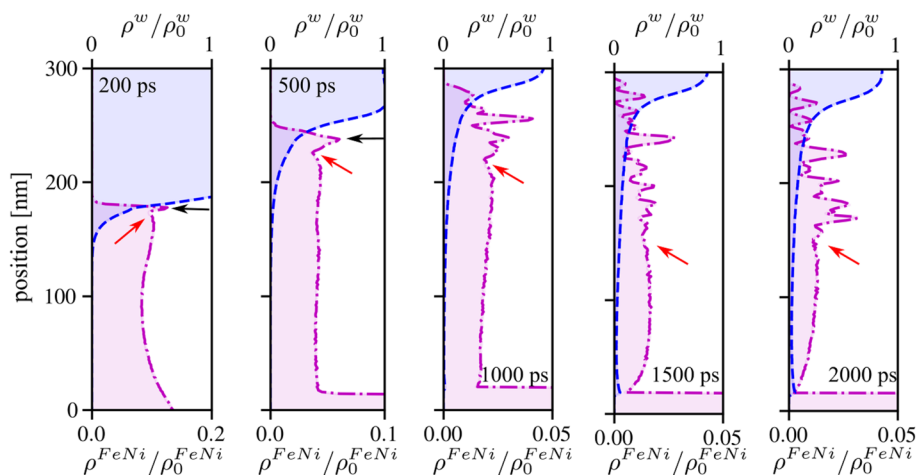


Fig. 18 The evolution of the density profiles in the ablation plume (dot-dashed magenta lines) and water (dashed blue lines) predicted in a simulation of PLAL of a FeNi target irradiated by a 10 ps laser pulse at an absorbed fluence of 3000 J/m². The density of the FeNi plume is normalized by the density of FeNi crystal at 300 K, ρ_0^{FeNi} , and the density of water is normalized by the room temperature water

density, ρ_0^w . The black arrows mark the high-density layer transiently formed at the plume-liquid interface during the initial plume expansion. The red arrows mark the location of the phase decomposition front that approximately follows the $0.8T_c$ isotherm. Note the changes in the scale of the plume density between the panels

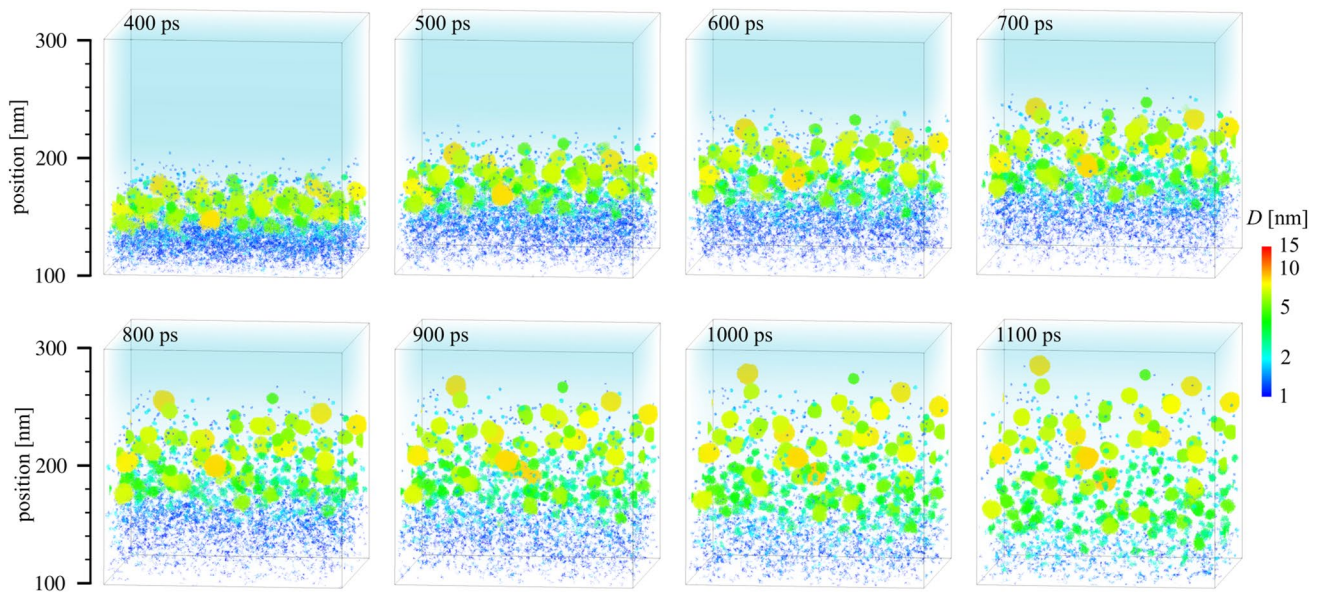


Fig. 19 The enlarged views of the interfacial region in a simulation illustrated in Fig. 17, with atoms colored by size (equivalent diameter D) of the NPs they belong to. The vapor-phase atoms and atomic

clusters ($D < 1$ nm) are blanked. The snapshots highlight the formation and broadening of a layer of NPs at the plume-liquid interface at the second stage of the ablation process discussed in the text

arrows in Fig. 18 mark the locations where this temperature is reached. Below the red arrows, the plume remains largely homogeneous, while above the arrows the appearance of multiple density peaks reflects the decomposition of the plume into vapor and nanodroplets.

The density of the homogeneous part of the plume, however, is not constant but decreases with time. This decrease can be largely attributed to the redeposition of the plume to the target surface rapidly cooled by the electron heat conduction to the bulk of the target. The absorption of a large amount of the supercritical and, after 1.5 ns, close-to-critical plume by the target surface is clearly reflected by the steep decrease in the density of the plume in the vicinity of the surface observed in the density profiles shown in Fig. 18 for 1.5 and 2 ns.

The propagation of the front of the phase decomposition leading to the generation of NPs can be clearly seen from the spatially resolved NP size distributions shown in Fig. 20. At the first stage of the plume expansion, the NPs with sizes from 2 to 8 nm form within a narrow top layer of the plume that gets in contact with the liquid environment and cools down below $0.8T_c$, as can be seen from the distribution for 500 ps in Fig. 20a. As time progresses, some of the large NPs diffuse into the low-density vapor region formed due to the heating of the liquid environment, and the generation of new NPs closely follows the phase decomposition front defined by $0.8T_c$ isotherm propagating toward the target surface. Since the density of the supercritical plume decreases with time (Fig. 18), the new nanoparticles formed through

the phase decomposition tend to be smaller than the ones formed at the dense plume-liquid interface.

Note that the identification of atomic clusters and small NPs with sizes less than 1.5 nm (first three rows of pixels in Fig. 20) within the part of the plume that remains in the supercritical state is reflecting the appearance of density fluctuations within the supercritical fluid [54, 83] rather than the presence of stable clusters and NPs. The cluster identification algorithm [82] considers the atoms that are closer than a cutoff distance of 0.35 nm to each other to belong to the same cluster or NP, leading to mistaking the momentary atomic configurations in the dense parts of the supercritical fluid for clusters or NPs. As the density of the supercritical part of the plume decreases (Fig. 18), the size and the number of such transient clusters decrease as well (cf. distributions for 500 and 1000 ps in Fig. 20). The small 1 – 1.5 nm NPs are still present in front of the $0.8T_c$ isotherm, in the expanding region where the temperature is between T_c and $0.8T_c$.

The mass-weighted NP size distributions, shown in Fig. 21 for 300, 500, 1000, and 1500 ps, exhibit pronounced bimodal shapes, particularly at the initial stage of the ablation process, at 300 and 500 ps. As discussed above, the dominant contribution to the first two bins of the histogram ($D < 2$ nm) is coming from the part of the ablation plume that remains in the supercritical state. At 300 ps, the first bin ($D < 1$ nm) accounts for about 85% of the plume, while the NPs with $D > 2$ nm constitute less than 6% of the plume. As time progresses, the phase

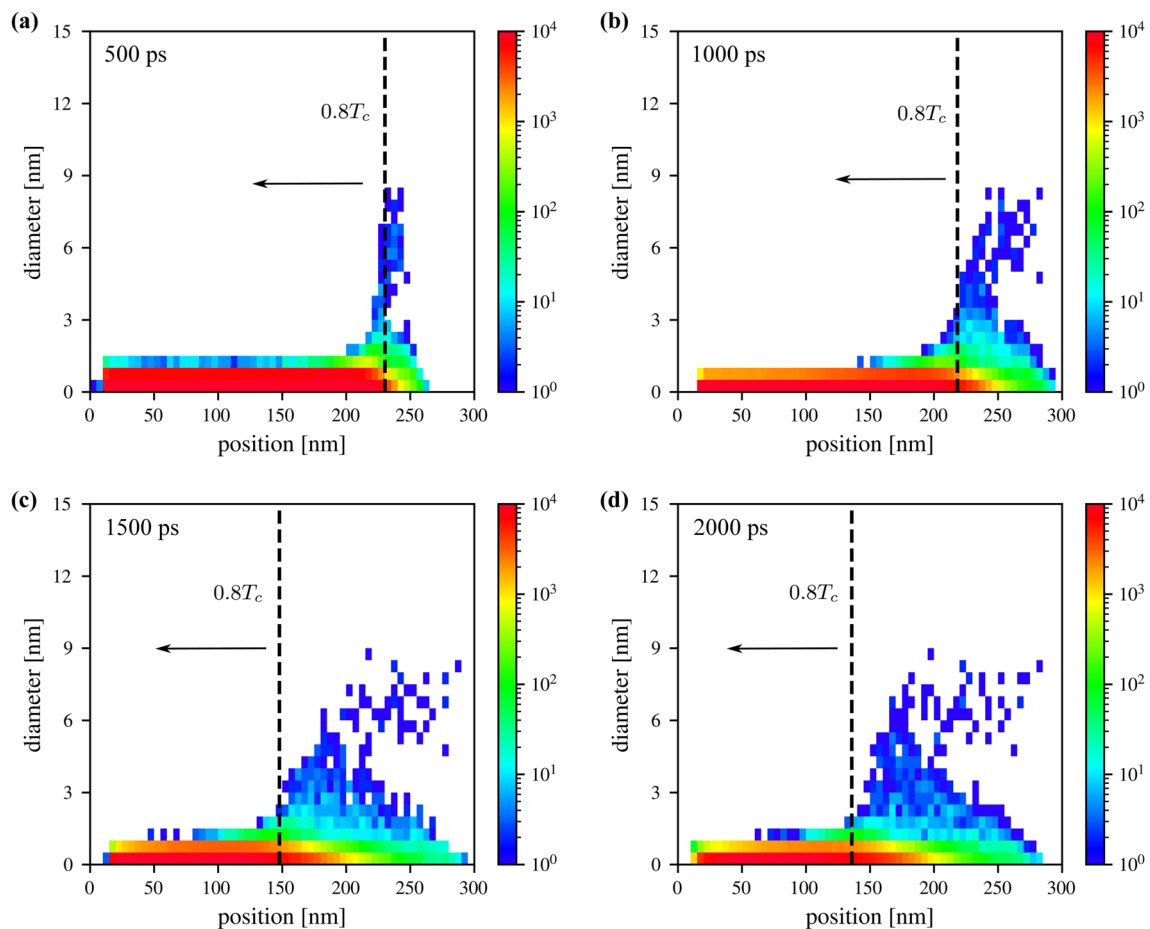


Fig. 20 Distributions of NPs of different sizes in the ablation plume calculated for 500, 1000, 1500, and 2000 ps in the simulation performed at $F_{\text{abs}} = 3000 \text{ J/m}^2$. The rectangular pixels are colored based on the number of clusters or NPs at locations and within the particle

size ranges defined by the x - and y -axes, as explained in the caption of Fig. 9. The vertical dashed lines show the locations of $0.8T_c$ isotherm that separates the homogeneous plume from the region containing NPs and vapor

decomposition from the supercritical state increases the fraction of the NPs and decreases the fraction of individual atoms and atomic clusters. The equivalent depths of NPs with $D > 2 \text{ nm}$ at 300, 500, 1000, and 1500 ps are 0.73, 0.75, 1.03, and 1.18 nm, respectively, while for the atoms and small clusters the equivalent depths are 11.11, 8.57, 3.90, and 2.16 nm, respectively. Similar to the results discussed in Sect. 3.4 for $F_{\text{abs}} = 1500 \text{ J/m}^2$, there is an imbalance between the increase in the mass of the large NPs and the decrease in the mass of the individual atoms, clusters, and small NPs. The latter decreases more rapidly due to the redeposition to the target surface.

It is interesting to note that the maximum size of the NPs at $F_{\text{abs}} = 3000 \text{ J/m}^2$ ($D < 9 \text{ nm}$ in Fig. 21) is smaller than that at a twice lower $F_{\text{abs}} = 1500 \text{ J/m}^2$ ($D < 12 \text{ nm}$ in Fig. 15). In both cases, the large NPs are formed through the phase decomposition from the supercritical state, and the sizes of the NPs are controlled by the density of the supercritical plume. A more vigorous initial expansion of the ablation

plume originating from a higher temperature surface region of the target leads to a larger initial decrease of the plume density at a higher fluence. Moreover, the slower propagation of the phase decomposition front in the higher-energy plume is allowing for an additional plume density reduction due to the redeposition to the target. One can expect that this trend will continue at fluences higher than 3000 J/m^2 , leading to further reduction of the density of the laser-induced supercritical plume and the corresponding decrease in the size of the NPs generated through the phase decomposition from the supercritical state.

3.6 Nanoparticles: cooling rates and solidification

The NPs produced in different parts of the ablation plume experience different thermal histories, largely defined by the surrounding environment. Those formed at the front of the expanding plume find themselves surrounded by water vapor, which facilitates rapid cooling of the molten NPs.

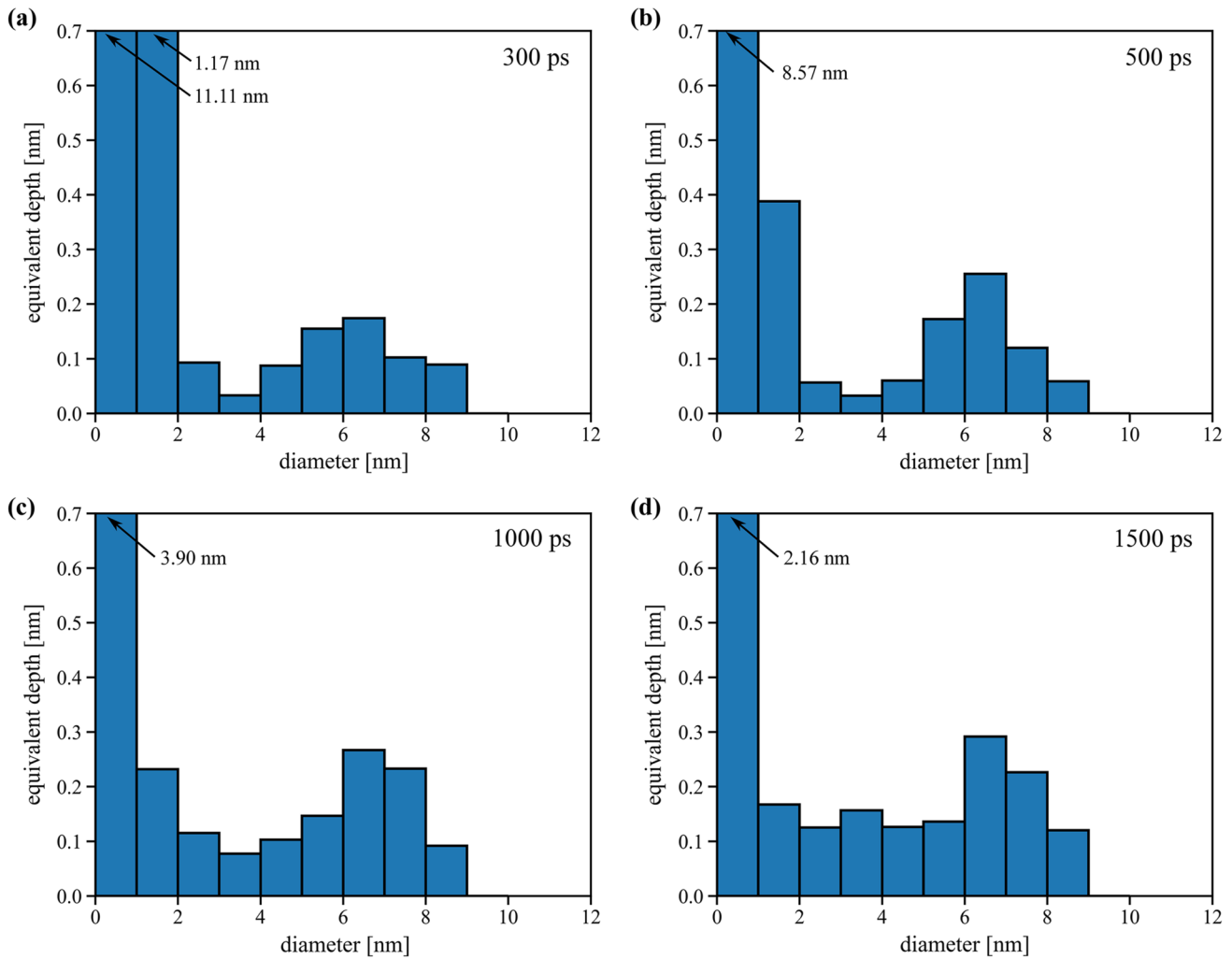


Fig. 21 Mass-weighted size distributions of atomic clusters and NPs predicted in a simulation performed at $F_{\text{abs}} = 3000 \text{ J/m}^2$ for times of 300, 500, 1000, and 1500 ps. The size of a NP or a cluster is characterized by the equivalent diameter D of a spherical particle consisting of the same number of atoms. The amount of target material converted to clusters or NPs within the size range of each bin is

expressed in terms of the equivalent depth of a surface layer of the initial target that contains the same number of atoms. The individual metal atoms are included in the first bin of the histograms. The summation over all bins gives the total ablation yield (expressed in terms of ablation depth) at a given moment of time

Moreover, some of the NPs are propelled into the dense and cold liquid environment at or above the boundary of the expanding cavitation bubble at the initial dynamic stage of the ablation process. Other NPs may diffuse into this cold environment after their formation through the decomposition of the interfacial layer. These NPs are the ones that undergo the fastest cooling and solidification on the time-scale of nanoseconds, i.e., within the timespan considered in the simulations.

The process of rapid cooling and solidification of NPs generated in the top part of the ablation plume is visualized for a simulation performed at $F_{\text{abs}} = 3000 \text{ J/m}^2$ in Fig. 22. The NPs in the snapshots are colored according to their temperature, and the individual atoms and atomic clusters with

$D < 1 \text{ nm}$ are blanked to provide a clear view of the NPs. The timespan covered in Fig. 22 corresponds to the third stage of the ablation process discussed in Sect. 3.5. At this stage, new NPs are generated at the phase decomposition front that follows the $0.8T_c$ isotherm (shown schematically by the dashed arrows crossing the snapshots), while the dense layer of NPs formed at the front of the ablation plume is spreading due to the Brownian motion of NPs in the interfacial region. Some of these NPs end up in the dense water region, as can be seen from the location of the top metal density peaks in the profiles shown in Fig. 22 for 1700 ps. These particles cool rapidly (turn blue in the snapshots shown in Fig. 22) and solidify under conditions of deep undercooling below T_m . Even earlier, small NPs formed through condensation in

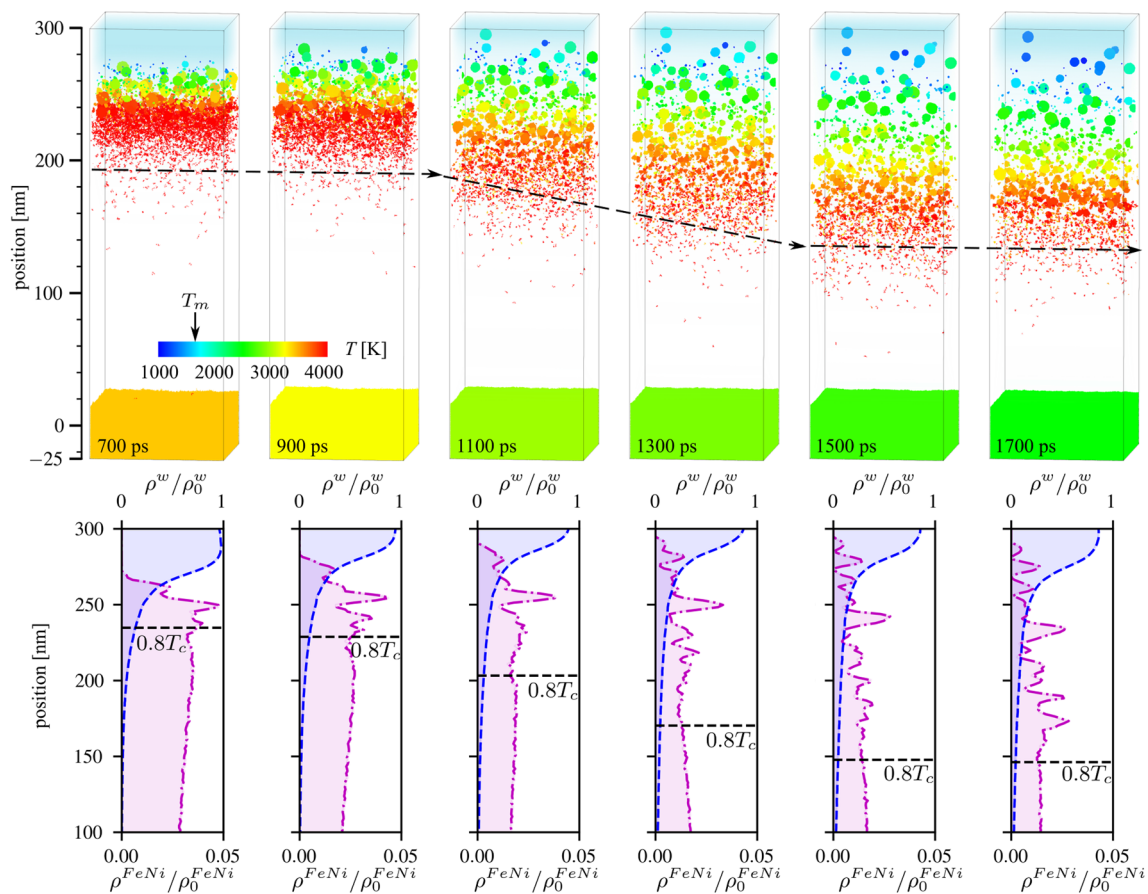


Fig. 22 Snapshots (upper row of panels) and density profiles (lower row of panels) from the third stage of the simulation of PLAL of FeNi target performed at $F_{\text{abs}} = 3000 \text{ J/m}^2$ and discussed in Sect. 3.5. The atoms in the snapshots are colored by the average temperature of NPs they belong to. Small clusters with $D < 1 \text{ nm}$ and individual atoms are blanked to provide a clear view of the NPs. The melting temperature of bulk FeNi alloy, T_m , is marked on the temperature scale. The density profiles for the ablation plume (magenta dash-dotted line) and water (blue dashed line) are normalized by the den-

sity of FeNi crystal at 300 K, ρ_0^{FeNi} , and the room temperature water density, ρ_0^w , respectively. The locations of the phase decomposition front that approximately follows the $0.8T_c$ isotherm are schematically shown by the black dashed arrows passing across the snapshots and are also marked by the horizontal dashed lines in the plots of the density profiles. The phase decomposition front separates the region containing homogenous plume from the region containing nanoparticles and vapor

the low-density vapor mixing region (the mechanism of NP formation observed at all fluences considered in the simulations) are also cooled below T_m and solidify. Some of these small NPs are already colored blue in the snapshot shown in Fig. 22 for 700 ps.

The cooling rates experienced by NPs generated by PLAL are illustrated in Fig. 23 for the three simulations discussed in Sects. 3.3, 3.4, and 3.5. The temperatures and positions of the 50 largest NPs identified at the end of each simulation are calculated by averaging over atoms that end up in each NP. The averaging is extended to the early stage of the ablation process, prior to the formation of the NPs, when the temperature evolution reflects the cooling of the material from the supercritical state leading to the phase separation and formation of NPs. Four representative NPs are selected in each simulation to illustrate the dependence of the thermal

history of a NP on its location in the ablation plume. The trajectories of the representative NPs are highlighted by color, with red, green, orange, and blue colors used for NPs ordered from higher to lower positions in the ablation plume.

From the temperature plots, we see that the NPs located closer to the target and further away from the plume-liquid interface (blue curves in Fig. 23) have higher temperatures and experience relatively slow cooling. The NPs generated in the top part of the plume are cooled more rapidly, with particularly high cooling rates observed for NPs embedded in the dense and cold liquid environment. The thermal history of such NPs is exemplified by the red curve in Fig. 23c, which corresponds to the topmost large NP visible in the last snapshot in Fig. 12, the upper peak in the plume density profile at 2 ns in Fig. 13, and the blue pixel at $D = 6.5 \text{ nm}$ and position of 155 nm in the distribution shown for 2 ns in

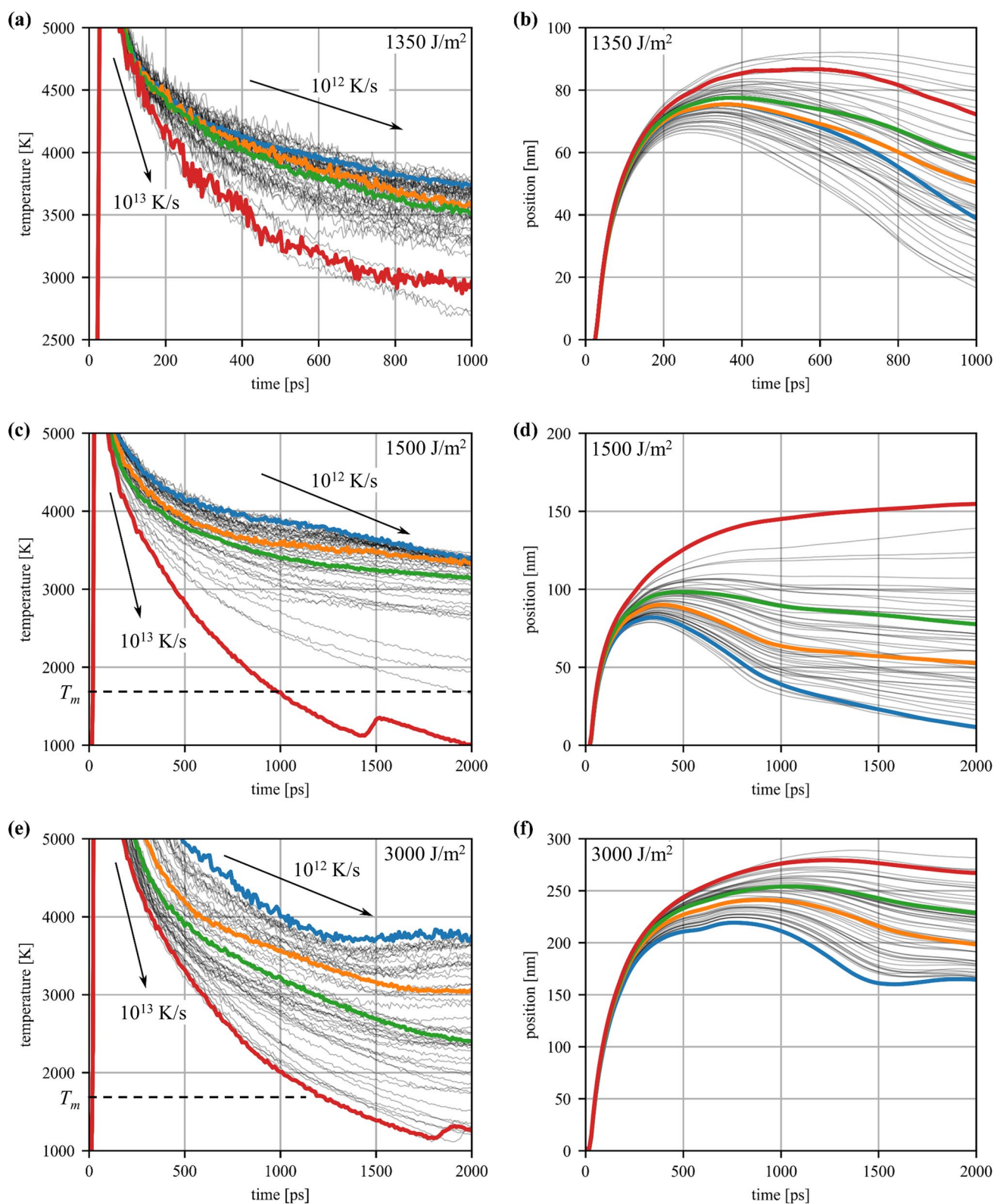


Fig. 23 The time dependence of the average temperatures and positions of groups of atoms that end up in the 50 largest NPs generated in the simulations performed at absorbed fluences of 1350 J/m² (a, b), 1500 J/m² (c, d), and 3000 J/m² (e, f). The plots for four representative NPs are highlighted by thicker blue, orange, green, and red

curves for each fluence. The arrows in the temperature plots have slopes that correspond to the cooling rates of 10^{12} and 10^{13} K/s, as marked in the figure. The horizontal dashed lines in (c, e) mark the equilibrium melting temperature of the target material

Fig. 14. The quench rate for this NP remains above 10^{12} K/s until it is undercooled down to $0.67T_m$ by the time of 1430 ps. Such deep undercooling triggers a rapid solidification of the NP, as indicated by the bump on the temperature plot appearing due to the reheating of the NP by the release of the latent heat of melting. This NP, therefore, solidifies just 1.5 ns after the laser irradiation.

Similarly fast quenching is observed for NPs generated at the plume-liquid interface in the simulation performed at a twice higher absorbed fluence of 3000 J/m^2 , where the NPs that diffuse into the dense liquid environment are cooled down rapidly (Fig. 22) and start to solidify at about 1.8 ns, as can be seen from the bump appearing on the red curve in Fig. 23e. While only a few large NPs solidify by the end of the simulation at 2.1 ns, the shapes of the temperature curves located between the red and green ones in Fig. 23e suggest that many more NPs will reach the critical level of undercooling required for the rapid solidification within the next several nanoseconds. The temperatures of the NPs in the lower part of the plume (temperature curves between the green and blue ones), however, plateau or even slightly increase after 1.5 ns due to the absorption of atoms and clusters from the adjacent supercritical fluid.

The temperatures of most of the large NPs in the simulation performed at 1350 J/m^2 are still significantly higher than T_m and, with the gradually decreasing cooling rates (Fig. 23a), it may take tens to hundreds of nanoseconds for them to reach the temperature levels required for the onset of homogeneous crystallization. This observation can be explained by the absence of large NPs in the vicinity of the outer boundary of the cavitation bubble, as evident from

the snapshots shown in Figs. 7 and 8. The large NPs formed through the roughening and decomposition of the interfacial molten layer (see Sect. 3.3) are moving down during the collapse of the spongy structure and redeposition of the molten layer (Fig. 23b) and end up well separated from the cold liquid environment. Note that a similar NP formation mechanism in PLAL of Ag targets is found to result in the injection of large NPs into the dense liquid environment through a sequence of hydrodynamic instabilities at the plume-liquid interface [17, 18]. The absence of these processes in the simulation of FeNi targets is related to a stronger localization of the energy deposition and formation of a thinner interfacial layer, as discussed in Sect. 3.3.

An important implication of the rapid quenching of NPs and the solidification occurring under conditions of strong undercooling is the generation of a high density of crystal defects in the solidified NPs. The generation of crystal defects is exemplified in Fig. 24 for a NP with $D = 6.82 \text{ nm}$ (15,556 atoms) that corresponds to the red curves in Fig. 23e, f. At 1800 ps, the temperature of the NP decreases to $0.69T_m$, but the NP still remains in the liquid state. The common neighbor analysis implemented in OVITO [84, 85], however, already identifies the presence of a small nucleus of atoms with a local structural environment that corresponds to the face-centered cubic (fcc) and hexagonal close packed (hcp) crystal structures. These atoms are colored green and red, respectively, while the atoms with the disordered local environment (*e.g.*, liquid-phase or surface atoms) are blanked in all but the first snapshots shown in Fig. 24. The crystalline nucleus rapidly grows and merges with the second nucleus that forms at 1820 ps. The solidification

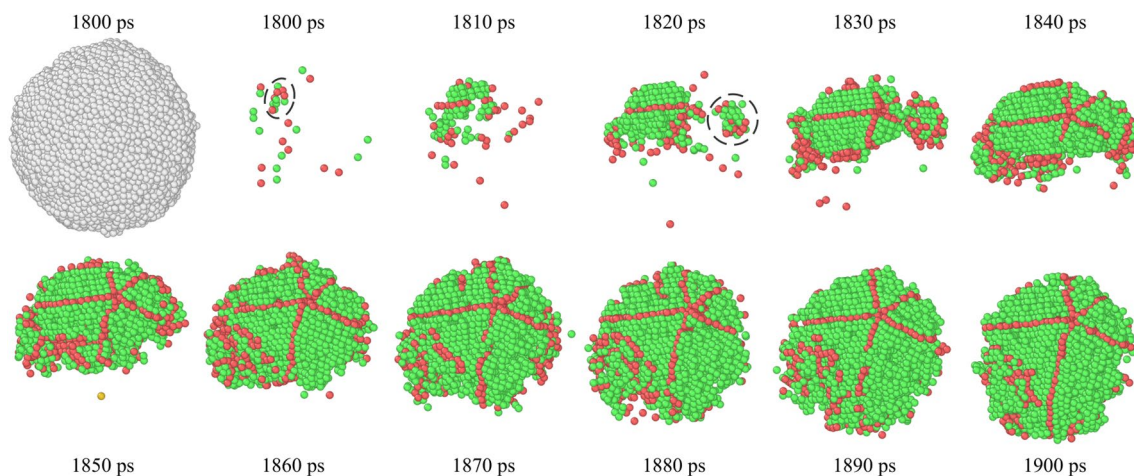


Fig. 24 Generation of crystal defects during the crystallization in a NP located in the top part of the ablation plume in a simulation performed at $F_{\text{abs}} = 3000 \text{ J/m}^2$. The evolution of temperature and position of the NP is shown by the red curves in Fig. 23e, f. In the first snapshot shown for 1800 ps, all atoms of the NP are represented by grey spheres. In all other snapshots shown for different moments of time,

the atoms with local fcc and hcp surroundings are colored green and red, respectively, and all other atoms are blanked. With this coloring scheme, the planes of red atoms separating green regions correspond to coherent twin boundaries in the fcc structure. The dashed ellipses at 1800 and 1820 ps outline the regions where new crystallites nucleate during the solidification

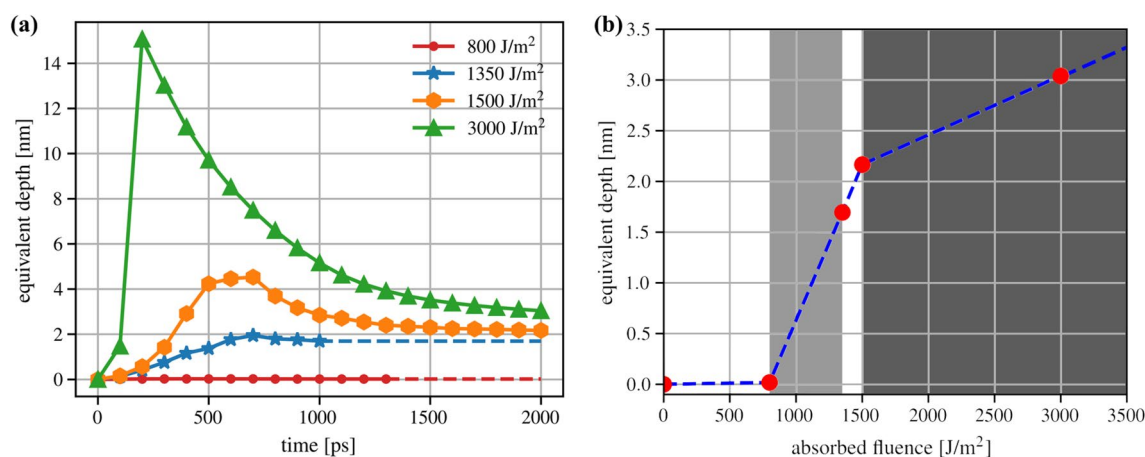


Fig. 25 The time dependence of the total amount of material ejected from the target (i.e., ablation yield) at fluences of 800, 1350, 1500, and 3000 J/m² (a) and the ablation yield as a function of absorbed fluence at the end of the simulations (b). The ablation yield is expressed in terms of the equivalent depth of a surface layer of the initial target that contains the same number of atoms. In (a), the data points connected by solid lines are the results of the simulations, and the dashed lines are extrapolations beyond the time of the simulation. In (b), the light grey region corresponds to the steep increase in the ablation

yield upon the transition of the NP formation mechanism from the surface evaporation and condensation at $F_{\text{abs}} = 800$ J/m² to the decomposition of the surface layer of the target transiently heated above T_c at $F_{\text{abs}} = 1350$ J/m². The dark grey region corresponds to the slower increase of the ablation yield in the regime where the NP generation through the phase separation from the supercritical state proceeds simultaneously with the redeposition of the plume to the target surface. The ablation yield between the red data point in (b) is approximated by linear interpolation, as shown by the dashed blue lines

completes at about 1900 ps and produces a defect-rich NP featuring five twin boundaries joining together along a common $\langle 110 \rangle$ direction in the adjacent fcc crystallites. With the coloring scheme based on the local structure analysis, a coherent twin boundary appears as a single plane of hcp (red) atoms separating fcc (green) crystallites. The pentagonal twinned configuration is produced by a self-replicating growth twinning occurring under conditions of rapid non-equilibrium solidification [86–88]. It can be described as a positive partial wedge disclination [89, 90] with a strength (Frank vector) equal to 7.35° . The elastic strain produced by the disclination and the surface states associated with the twin boundaries are among the factors that are likely to be responsible for the enhanced catalytic activity of NPs generated in PLAL experiments [19–21].

3.7 Nanoparticles: total yield and size distributions

The computational predictions on the evolution of the total amount of material ejected from the target during the ablation process and the final yield of NPs are summarized in Fig. 25 for different regimes of PLAL discussed in Sects. 3.1–3.5. The total amount of ejected material is defined with the help of cluster analysis [82] that makes it possible to distinguish the ablation plume from the liquid structures connected to the bulk of the target. This distinction is not trivial, as one can see from the snapshots colored by the size of the NPs shown for $F_{\text{abs}} = 1350$ J/m² in Fig. 8. The spongy liquid structure does not separate from the

target at any time during the simulation and, therefore, does not contribute to the ablation yield. The gradual increase in the ablation yield with time observed for this fluence in Fig. 25a is defined by the evaporation and condensation of metal atoms in the low-density water-metal mixing region occurring simultaneously with roughening of the top part of the spongy structure and its decomposition into larger NPs. The moderate decrease in the total yield after the collapse of the spongy structure is due to the redeposition of some of the NPs and atomic clusters to the target surface.

The much larger increase of the total yield at the initial stage of the ablation process observed for $F_{\text{abs}} = 1500$ J/m² is related to the splitting of the ablation plume into a lower spongy part that remains connected to the target and an upper part forming a packet of supercritical fluid that pushes against the liquid environment. A top part of the upper supercritical region decomposes into vapor and nanodroplets upon interaction with the liquid environment, while a substantial part of it reflects from the liquid environment and redeposits to the target after 700 ps. The redeposition is responsible for the decrease in the amount of material in the ablation plume after 700 ps that can be seen for this fluence in Fig. 25a.

The redeposition has an even more dramatic effect on the total yield in the simulation performed at $F_{\text{abs}} = 3000$ J/m², where the whole plume is brought into the supercritical state, and the NPs are generated at the phase decomposition front slowly propagating from the liquid-plume interface toward the target surface. A major part (about 80%) of the

material brought into the supercritical state and ejected from the target during the first 200 ps of the ablation process is redeposited to the target surface by the time of 2 ns. As a result, the NP yield at the end of the simulation is only about 40% higher than that observed in the simulation performed at a twice lower absorbed fluence of 1500 J/m².

The fluence dependence of the total ablation yield recorded at the end of the simulations is shown in Fig. 25b, where three distinct regimes of PLAL can be identified. At low fluences, $F_{\text{abs}} \leq 800 \text{ J/m}^2$, the material ejection and NP formation are limited to the evaporation–condensation process, the time when the evaporation takes place is short due to the rapid cooling of the target surface, and the ablation yield remains very small. Above 800 J/m², in the region highlighted by the light grey color, the interface between the hot molten layer accumulated at the front of the ablation plume and the liquid environment becomes unstable during the initial plume expansion. The roughening of the interface leads to the formation of large NPs, which leads to a significant increase in the total ablation yield.

The absorbed fluence of 1500 J/m² is the threshold for the separation of the supercritical part of the plume from

the spongy structure connected to the target, and the phase decomposition of the top part of the supercritical cloud of material upon contact with the liquid environment gives an additional boost to the total ablation yield. The transition to the formation of a long-living supercritical plume upon further increase of absorbed fluence, however, leads to a sharp increase in the fraction of the initial plume redeposited to the target, Fig. 25a, and results in a weaker fluence dependence of the ablation yield in the regime highlighted by dark gray color in Fig. 25b.

The fluence dependence of the ablation yield suggests that despite the continuous increase in the total ablation yield with increasing fluence, the optimum energy efficiency of the NP synthesis is realized close to the threshold for the formation of the supercritical ablation plume, i.e., around 1500 J/m². Indeed, since doubling the absorbed fluence from 1500 to 3000 J/m² results in a 40% increase in the ablation yield, the ablation efficiency defined as a ratio of ablation yield to the deposited energy decreases by 30%. As discussed below, in Sect. 3.8, the computational prediction of the ablation efficiency going through a maximum and decreasing at higher fluences is

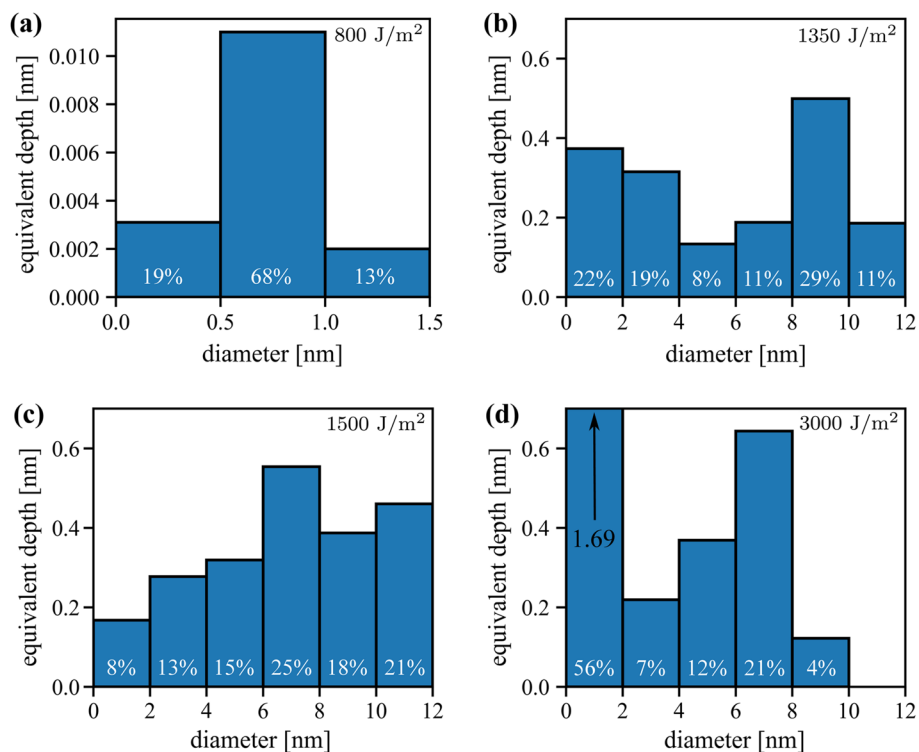


Fig. 26 Mass-weighted size distributions of atomic clusters and NPs predicted in simulations performed at absorbed fluences of 800 J/m² (a), 1350 J/m² (b), 1500 J/m² (c), and 3000 J/m² (d). The distributions are calculated for times of 1300 ps for 800 J/m², 1000 ps 1350 J/m², and 2000 ps for 1500 and 3000 J/m². The size of a NP or a cluster is characterized by the equivalent diameter D of a spherical particle consisting of the same number of atoms. The amount of target mate-

rial converted to clusters and/or NPs within the size range of each bin is expressed in terms of the equivalent depth of a surface layer of the initial target that contains the same number of atoms. The individual metal atoms are included in the first bin of the histograms. The summation over all bins gives the total ablation yield (expressed in terms of ablation depth) at a given moment of time. The white labels show the relative weight fractions represented by each bin

in agreement with trends observed in PLAL experiments [91, 92].

Beyond the total NP yield and the energy efficiency, an important consideration in the NP synthesis by PLAL for practical applications is the NP size distribution. The size distributions are defined by the mechanisms of the NP generation and exhibit different characteristics in the three fluence regimes discussed above. The mass-weighted NP size distributions are shown for the absorbed fluences of 800, 1350, 1500, and 3000 J/m² in Fig. 26. In the low fluence regime, exemplified by $F_{\text{abs}} = 800 \text{ J/m}^2$, the evaporation – condensation mechanism produces atomic clusters and small NPs with sizes below 1.5 nm. While the atomic clusters and small NPs are in high demand for practical applications due to their unique optical properties [93] and catalytic activity [94, 95], the low total yield (equivalent depth of the target converted to the clusters and NPs is less than 0.02 nm) makes NP/cluster synthesis in this regime of PLAL highly inefficient.

The transition to the medium fluence regime not only leads to a sharp increase in the total ablation yield but also drastically changes the NP size distribution, as illustrated in Fig. 26b, c for absorbed fluences of 1350 and 1500 J/m². At both fluences, the mass-weighted size distributions are dominated by large NPs with diameters ranging from 4 to 12 nm, with the fraction of such NPs increasing from 59% at $F_{\text{abs}} = 1350 \text{ J/m}^2$ to 79% at 1500 J/m². The transition from the generation of large NPs through the interface roughening at $F_{\text{abs}} = 1350 \text{ J/m}^2$ to the decomposition of the dense layer of supercritical fluid at 1500 J/m² results in a significant increase in the fraction of the largest NPs with $D > 10 \text{ nm}$.

Interestingly, a further increase of the absorbed fluence to $F_{\text{abs}} = 3000 \text{ J/m}^2$ eliminates the largest NPs from the distribution, Fig. 26d. In particular, the NPs with $D > 10 \text{ nm}$ account for 21% of the total mass of the ablation plume at 1500 J/m² but are completely absent at $F_{\text{abs}} = 3000 \text{ J/m}^2$. At this high fluence, a significant part of the ablation plume has not undergone the phase separation by the end of the simulation and still remains in the homogeneous close-to-critical state between $0.8T_c$ and T_c , Fig. 16. This part of the plume contributes to the first bin of the histogram in Fig. 26d, accounting for more than half of the total mass of the ablation plume. While the phase decomposition in this part of the plume is expected to produce NPs with larger sizes, the low and decreasing density of this region (Fig. 18) suggests that the newly formed NPs are likely to have sizes below 6–7 nm. This conjecture is supported by the trend illustrated in Fig. 20, where the sizes of NPs generated at the phase decomposition front are decreasing with decreasing density of the homogeneous part of the plume. These observations suggest that while the high fluence irradiation regime may not be optimal from the energy efficiency point

of view, it has the advantage of producing a narrower size distribution with a lower maximum size of the NPs.

3.8 Maps of transient states generated by a Gaussian laser beam

The discussion of different regimes of laser ablation provided in previous sections is based on the results of simulations performed with periodic boundary conditions applied in the lateral directions, parallel to the surface of the target. These conditions provide an adequate description of the initial stage of laser ablation caused by a flat-top (also known as top-hat) laser beam irradiation, when the effect of the edges of the beam and the variation of the laser fluence across the beam can be neglected. Most of the PLAL experiments, however, are performed with spatially inhomogeneous laser beam profiles commonly assumed to have a Gaussian variation of the incident laser fluence [96, 97]. In this case, the mechanisms of the material ejection and NP formation identified in simulations performed for different absorbed laser fluences can be activated simultaneously in different parts of a laser spot and may collectively contribute to the ablation yield and the NP generation. To perform analysis of PLAL by a Gaussian laser beam, we use the “mosaic” approach illustrated in Fig. 1, where results of the simulations discussed in previous sections are mapped to different parts of the laser spot.

The variation of the absorbed laser fluence within a laser spot produced by a Gaussian laser beam can be described by the following equation:

$$F_{\text{abs}}(r) = (1 - R)F_{\text{in}} = (1 - R)F_{\text{in}}^{\text{peak}} \exp\left(-\frac{2r^2}{w_0^2}\right), \quad (1)$$

where R is the reflectivity of the target surface, r is the distance from the center of the laser spot, w_0 is the Gaussian laser beam radius at $1/e^2$ peak intensity of the beam, and $F_{\text{in}}^{\text{peak}}$ is the peak incident fluence at the center of the laser spot. Note that a significant deviation from the linear conversion of the incident fluence F_{in} to the absorbed fluence F_{abs} can arise from the dependence of R on the electron and lattice temperatures, particularly for short and ultrashort laser pulses [17, 98]. These deviations can distort the energy deposition profile with respect to the incident Gaussian profile but are neglected in the following discussion for simplicity.

To map the results of the simulations discussed in Sects. 3.1–3.5, we assume the maximum absorbed fluence in the center of the laser spot to be $F_{\text{abs}}^{\text{peak}} = 3000 \text{ J/m}^2$. Using Eq. (1), we can then associate absorbed fluences F_{abs} of 600, 800, 1350, and 1500 J/m² with the following distances r from the center of the laser spot: $0.90 w_0$, $0.82 w_0$, $0.63 w_0$, and $0.59 w_0$, respectively.

The next step is to convert the complex and detailed mechanistic information revealed in the atomistic simulations into simplified spatially and time-resolved maps of the transient phase states realized at different times and in different locations within the laser spot at the initial stage of PLAL. To facilitate this step, we distinguish the phase states of the target material based on the evolution of temperature and density illustrated by contour plots shown in Figs. 3, 6, 11, and 16.

The material is considered to be in a *solid state* if its density is within 10% of the density of FeNi at 300 K, ρ_0^{FeNi} . This criterion is found to provide reliable identification of the solid–liquid interface under conditions when the solid is laterally confined and undergoes an uniaxial expansion in the direction normal to the irradiated surface. This identification of the solid–liquid interface is also confirmed by the analysis of the local atomic structure.

To identify the single-phase regions of *molten metal*, and to distinguish them from those where the melt coexists with vapor or voids, we use a theoretical expression describing the temperature dependence of the equilibrium density of the molten metal [67],

$$\rho_l(T) = \rho_c + A_0(T_c - T)^\beta + A_1(T_c - T)^{\beta+\theta} + B_1(T_c - T) \tag{2}$$

and fit it to the properties of the model FeNi alloy. Fitting this equation to the results of liquid–vapor coexistence simulations [32] and assuming the theoretical values of exponents

$\beta = 0.326$ and $\theta = 0.54$ [67], the following parameters are obtained for the interatomic potential used in the present study: $\rho_c = 19.66 \text{ atoms/nm}^3$, $T_c = 4837 \text{ K}$, $A_0 = 2.601 \text{ atoms}/(\text{nm}^3 \cdot \text{K}^\beta)$, $A_1 = 3.608 \times 10^{-3} \text{ atoms}/(\text{nm}^3 \cdot \text{K}^{\beta+\theta})$, and $B_1 = 6.788 \times 10^{-3} \text{ atoms}/(\text{nm}^3 \cdot \text{K})$. The material that does not satisfy the density criterion for solid phase and has a local density within 20% of $\rho_l(T)$ is identified as a single-phase molten metal. The extension of the density criterion for the molten phase down to $0.8 \rho_l(T)$ makes it possible to account for the complex structure of the molten layer transiently formed in the medium fluence regime, e.g., Figs. 7 and 12 for absorbed fluences of 1350 and 1500 J/m², respectively.

The parts of the ablation plume where the local temperature is higher than T_c are identified as regions where the metal is in the *supercritical state*. The parts of the plume where the density is more than 20% below $\rho_l(T)$ and the temperature is below T_c , can either correspond to a spongy structure of interconnected liquid regions or a part of the plume decomposed into NPs and vapor. The spongy structure has a temperature below $0.9T_c$ and, under the conditions of the simulations reported in this paper, is always generated in the vicinity of the target. Therefore, the *spongy structure* is identified as a part of the system that is located below either a molten layer or a supercritical fluid region, has a density below $0.8 \rho_l(T)$ and a temperature below $0.9T_c$.

The regions above the supercritical or molten metal layers that have a density lower than $0.8 \rho_l(T)$ are categorized as *regions of NP formation*. The regions where the density

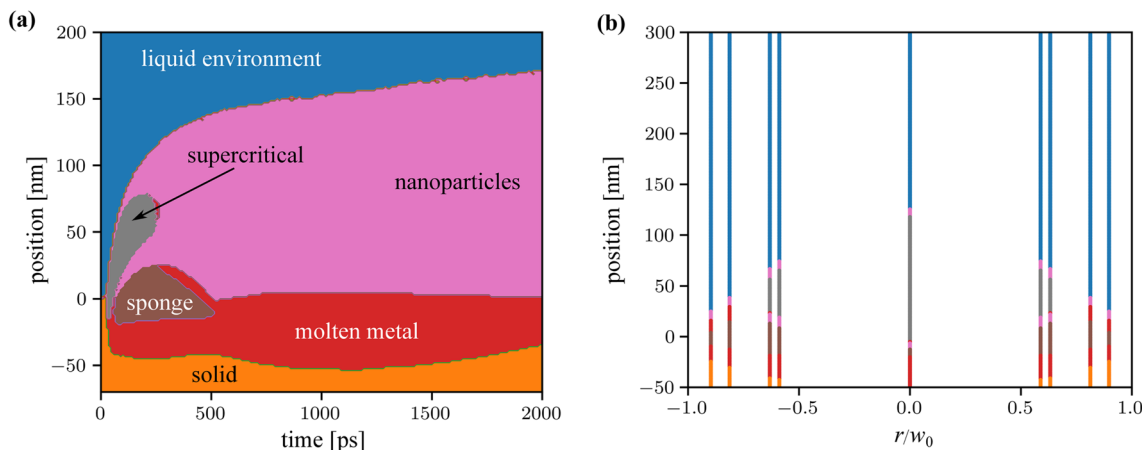


Fig. 27 Illustration of a method used for the identification of phase states at different times and in different parts of the ablation plume generated in PLAL by a laser beam with a Gaussian spatial profile. The contour plot in (a) shows the evolution of the states of the matter in a simulation performed for $F_{\text{abs}} = 1500 \text{ J/m}^2$. The states are identified based on the temperature and density plots shown in Fig. 11. The regions colored orange, red, and grey correspond to the solid, molten, and supercritical states of the target material. The region featuring spongy structure of interconnected liquid regions is colored brown.

The regions with conditions suitable for the NP formation are colored pink, and the liquid environment is colored blue. The results of the analysis performed for different fluences are then mapped to a Gaussian laser spot with a peak absorbed fluence of $F_{\text{abs}}^{\text{peak}} = 3000 \text{ J/m}^2$, providing a framework for reconstructing the evolution of the states of the matter during the ablation process, as illustrated for a time of 100 ps in (b). These frameworks, created for different times during the simulations, are used for the generation of phase state maps shown in Fig. 28

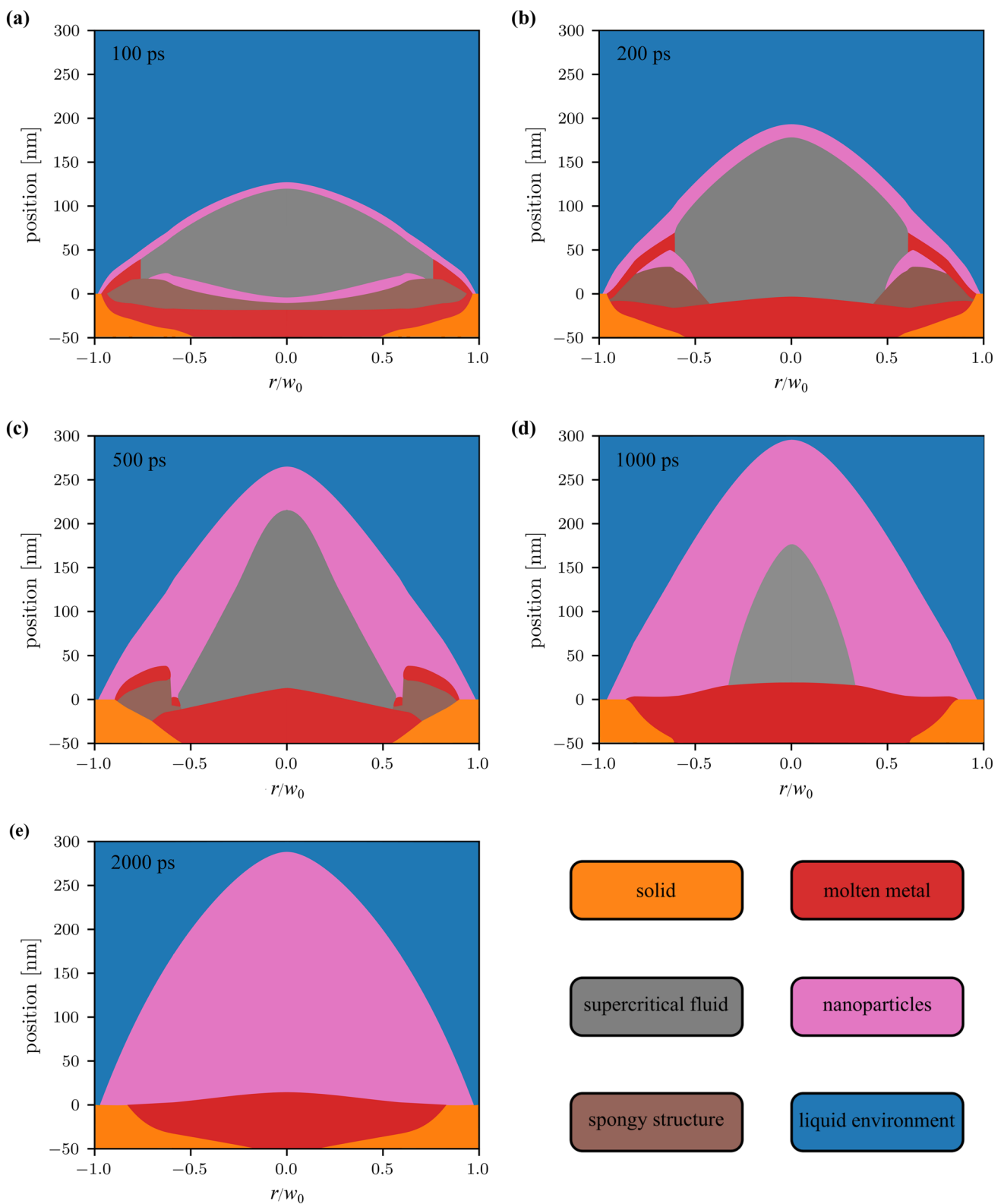


Fig. 28 The maps of the phase states present within the ablation plume generated by a laser beam with a Gaussian spatial profile with a beam radius w_0 at $1/e^2$ peak intensity of the beam and a peak absorbed laser fluence of 3000 J/m^2 . The phase maps are based on analysis of the density and temperature distributions predicted in atomistic simulations discussed in Sects. 3.1–3.5 and are shown for times of 100, 200, 500, 1000, and 2000 ps after the laser pulse. The regions colored orange, red, and grey correspond to the solid, molten, and supercritical states of the target material. The regions featuring spongy structures of interconnected liquid regions are colored brown. The regions with conditions suitable for the NP formation are colored pink, and the liquid environment is colored blue. Note that typical diameters of laser spots are in the range of tens to hundreds of micrometers, and the images are shown with a large aspect ratio between the lateral and vertical dimensions to provide a clear view of distinct layers of the ablation plume, which remain essentially flat at this early stage of the ablation process

is below $0.8 \rho_1(T)$ and the local temperature is between $0.9T_c$ and T_c are also defined as regions of NP formation, regardless of the location of these regions. These regions are fairly homogeneous and correspond to the parts of the plume where the phase separation (NP formation) takes place upon further evolution of the ablation plume. Finally, the part of the system free of the metal atoms is identified as a *liquid environment* region.

Using the simple criteria described above, the data on the evolution of temperature and density in the simulations discussed in Sects. 3.1–3.5 are converted to the contour plots of the phase state. The results of this conversion are exemplified in Fig. 27a for a simulation performed at $F_{\text{abs}} = 1500 \text{ J/m}^2$. The phase map adequately captures the formation of a spongy structure in the lower part of the ablation plume and a supercritical region in the top part of the plume, the appearance and redeposition of a molten metal layer covering the spongy structure, and the evolution of the melting/solidification front in the target, as expected based on the contour plots and snapshots shown in Figs. 11 and 12. A similar analysis is performed for other fluences, and the cross-sections of the contour plots at different moments of time are mapped to the Gaussian laser spot, producing elements of “mosaics” of the phase states at different times during the ablation, as shown for a time of 100 ps in Fig. 27b.

Connecting the elements of the “mosaics” by extrapolating between the same phase states in the spatial maps plotted for different moments of time produces a sequence of snapshots of the laser ablation process occurring at the scale of the whole laser spot. These snapshots, or maps of the transient phase states, are provided in Fig. 28 for a laser spot irradiated by a laser beam with a Gaussian spatial profile and a peak absorbed fluence of $F_{\text{abs}}^{\text{peak}} = 3000 \text{ J/m}^2$.

The map shown in Fig. 28a for 100 ps illustrates the initial expansion of the material heated by the laser energy deposition and the formation of a layered structure in the laser-induced plume. The direct interaction of the top part

of the expanding plume with the liquid environment leads to a rapid cooling and formation of a very thin interfacial layer with temperature below T_c and conditions suitable for the nucleation and growth of atomic clusters and nanoparticles (the thin pink layer at the plume-liquid interface in Fig. 28a). Below the interfacial layer is a large region of the target material transformed to a dense supercritical phase (grey area in Fig. 28a) and a layer of a spongy structure of liquid regions (brown) connected to the molten pool generated within the laser spot (red). At the periphery of the laser spot, the spongy structure generated by a combined effect of the unloading of laser-induced pressure and the explosive phase decomposition of the superheated material [18] extends all the way to the interface with the liquid environment, where a layer of molten metal forms at the top of the spongy structure.

As time progresses to 200 and 500 ps, the supercritical region expands and pushes the liquid environment further away from the target surface, Fig. 28b, c. The interfacial region of the NP formation broadens due to the mixing with the liquid environment and cooling of the top part of the plume, while the spongy structure in the central part of the laser spot collapses due to the pressure exerted by the overlying supercritical part of the plume.

By the time of 1 ns, the remaining spongy structure at the periphery of the laser spot redeposits to the target, causing a transient remelting and widening of the melt pool, while the supercritical region further shrinks in the central part of the cavitation bubble, Fig. 28d. A large fraction of the plume is already converted into NPs by this time in the parts of the plume corresponding to medium fluence irradiation regime within the laser spot (see Sects. 3.3 and 3.4), while the decomposition of the supercritical plume into vapor and nanoparticles is still ongoing in the central part of the plume. The phase decomposition occurs simultaneously with rapid material redeposition from the supercritical region to the target surface, which decreases the density of the plume and the sizes of NPs produced at the phase decomposition front.

By the time of 2 ns, all regions of the ablation plume have already cooled below T_c , but the front of the phase separation into large droplets and vapor follows the $0.8T_c$ isotherm and is still located above the surface of the target. The size of the melt pool visibly shrinks between 1 and 2 ns, suggesting that complete resolidification of the target surface is likely to occur within the next 10 ns.

The computational prediction of the complex and rapidly evolving distribution of different phase states within the ablation plume produced at the early stage of PLAL provides an opportunity for making direct links to the results of time-resolved experimental probing of the ablation dynamics [24–29]. In particular, the maps of the phase states shown in Fig. 28 can be converted to maps of transient reflectivity

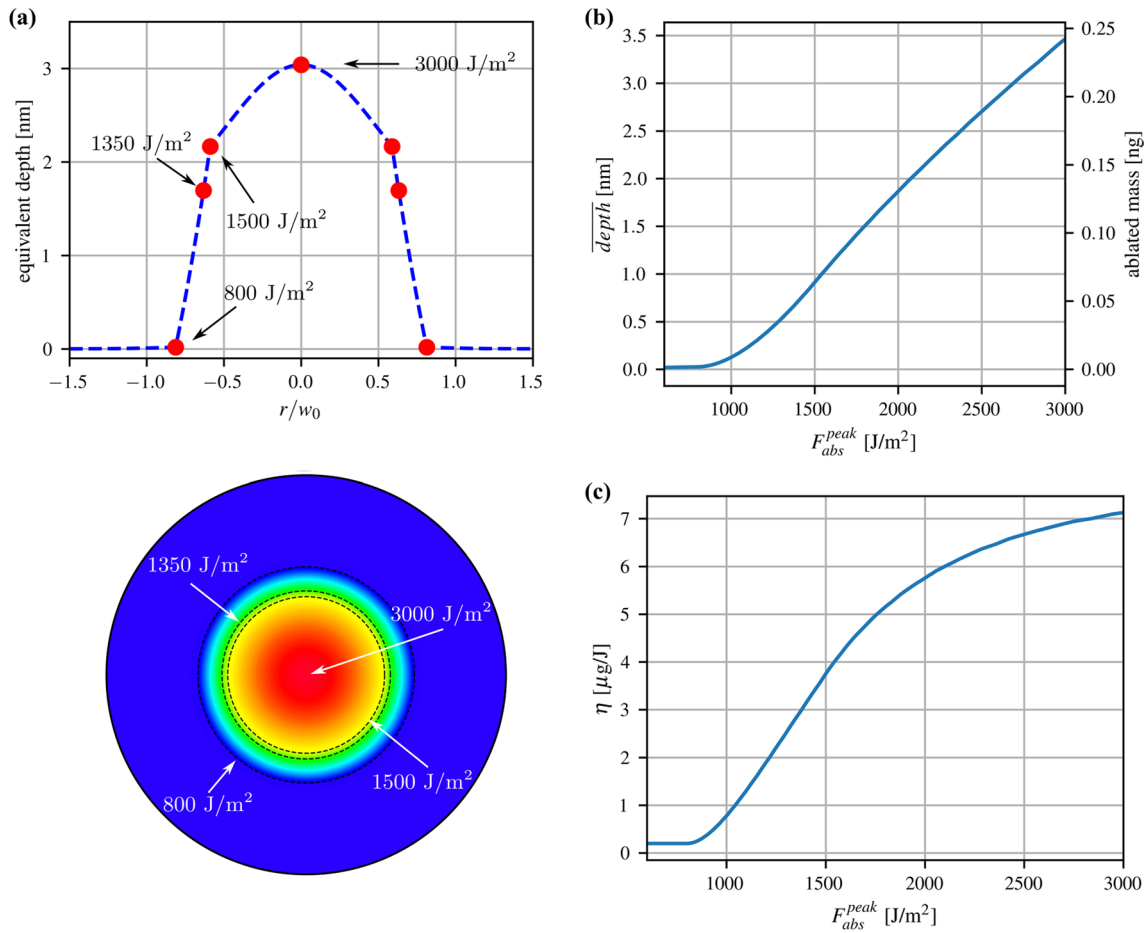


Fig. 29 Two representations of the distribution of local ablation depth $depth(r)$ within a laser spot with a Gaussian spatial profile predicted in the atomistic simulations (a), the total ablation yield ejected from the laser spot expressed in terms of the average equivalent depth \overline{depth} and the ablation mass M_a calculated for different values of the

peak absorbed fluence F_{abs}^{peak} (b), and the ablation energy efficiency η defined as the ratio of the ablated mass M_a to the absorbed laser energy E_{abs} (c). In the calculation of M_a , the FWHM spot size of 100 μm is assumed

measured in the ultrafast pump-probe microscopy imaging of the ablation dynamics [29]. The calculation of the optical signatures of different stages of the ablation process is the subject of our current work [37] and will be reported elsewhere.

The integral picture of the ablation process at the scale of the laser spot also allows for the evaluation of the total ablation yield produced by a single laser pulse with a Gaussian spatial beam profile. The fluence dependence of the ablation yield shown in Fig. 25b can be mapped to the Gaussian distribution of the absorbed fluence, as shown in Fig. 29a. The total mass of the ablation yield generated by the laser pulse, M_a , can be calculated by integration of the local ablation depth, $depth(r)$, over the area of the laser spot,

$$M_a = \rho \int_0^{2\pi} \int_0^\infty depth(r) r dr d\theta = \overline{depth} \times \rho \pi w_0^2 \ln(2)/2 \quad (3)$$

where ρ is the material density and \overline{depth} is the average equivalent ablation depth from a laser spot with a diameter defined as the full width at half maximum (FWHM) of the Gaussian profile, $d_{FWHM} = \sqrt{2 \ln 2} w_0$. Using the data on $depth(r/w_0)$ predicted in the simulations and plotted in Fig. 29a, the average equivalent depth \overline{depth} and the total ablation mass M_a can be calculated for different values of the peak absorbed fluence F_{abs}^{peak} , up to the maximum value considered in the simulations, 3000 J/m^2 . In this calculation, the value of w_0 is chosen so that $d_{FWHM} = 100 \mu\text{m}$, a typical value used in picosecond PLAL experiments [99]. The results of the calculation are provided in Fig. 29b, where M_a is seen to increase with the peak absorbed fluence up to 0.24 ng at the maximum peak fluence of 3000 J/m^2 considered in the simulations. The total mass of the ablation plume predicted in the simulations is within the range of values evaluated in picosecond PLAL experiments for Cu targets

in water performed for different laser focusing conditions, 0.1–0.55 ng per pulse [99].

In contrast to the dependence of the ablation depth on the local fluence (Fig. 25b), where there is a large decrease in the slope of the local fluence dependence of the ablation yield, the weakening of the dependence of the total ablation yield on the peak fluence (Fig. 29b) is less pronounced. This observation can be explained by the combined contribution to the total ablation yield from the peripheral parts of the laser spot exposed to the irradiation in the medium fluence regime, where the ablation yield exhibits a high sensitivity to the local fluence (light grey area in Fig. 25b), and the central area exposed to high local fluences, where the ablation yield has a weaker dependence on the local fluence (dark grey area in Fig. 25b). One can expect that the trend of weakening of the dependence of total ablation yield on the peak fluence in Fig. 29b will continue at higher peak fluences, beyond the maximum $F_{\text{abs}}^{\text{peak}} = 3000 \text{ J/m}^2$ considered in the atomistic simulations, due to the increased contribution of the less energy efficient ablation at higher fluences.

The saturation of the energy efficiency of the NP generation with increasing peak fluence is even more apparent from the analysis of the ablation efficiency η , defined as the ratio of the total ablation mass M_a to the total energy deposited by the laser pulse E_{abs} . The latter can be calculated as

$$E_{\text{abs}} = \int_0^{2\pi} \int_0^\infty F_{\text{abs}}^{\text{peak}} \exp\left(-\frac{2r^2}{w_0^2}\right) r dr d\theta = \frac{1}{2} \pi w_0^2 F_{\text{abs}}^{\text{peak}} \quad (4)$$

Within the range of laser fluences considered in the present study, the ablation efficiency plotted in Fig. 29c still increases with increasing fluence, although the slope of the curve is notably decreasing. Given the trend of the gradual saturation of the dependence of the ablation yield on the local fluence shown in Fig. 25b, the ablation energy efficiency η is expected to pass through the maximum and then decrease upon a further increase in the peak fluence. Similar fluence dependences of the ablation efficiency have been observed in PLAL experiments performed with picosecond [91] and nanosecond [91, 92] laser pulses.

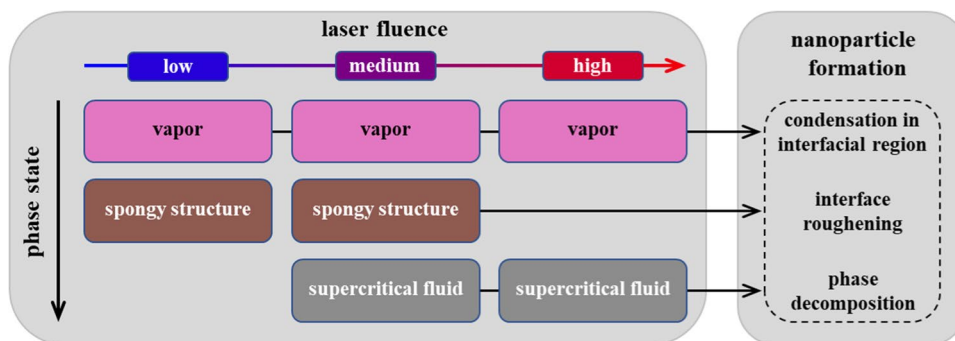
Quantitatively, the ablation energy efficiency predicted in the simulations shows signs of reaching the maximum level of slightly above $7 \mu\text{g/J}$ (Fig. 29c), which is comparable to the results of experimental measurements. In particular, the ablation energy efficiency is observed to increase up to about $4 \mu\text{g/J}$ in picosecond laser ablation of Au in water [91], while somewhat higher maximum values are reported for nanosecond PLAL, around $5 \mu\text{g/J}$ of Pd, Cu, and Ag in ethanol [92] and up to $12 \mu\text{g/J}$ for Au in water [91]. When comparing the computational values of the ablation yield and ablation efficiency to the experimental data, one should note the likelihood of a significant reduction of the ablation yield due to the redeposition to the target surface. While the most active dynamic stage of the ablation plume redeposition has largely ceased by the end of the simulations (Fig. 25a), additional slower but persistent redeposition can be expected during the long-term evolution and collapse of the cavitation bubble. The somewhat higher ablation efficiency predicted in the simulations as compared to the picosecond PLAL experiments, therefore, is consistent with the notion of the reduction of the ablation yield during the long-term evolution of the ablation plume confined within the cavitation bubble.

4 Summary

The mechanisms responsible for the material ejection and NP formation in PLAL are investigated in a series of large-scale atomistic simulations performed for FeNi targets irradiated by 10 ps laser pulses in a liquid environment. The simulations reveal the existence of three fluence regimes featuring different dominant mechanisms of the material ejection and NP formation, as schematically illustrated in Fig. 30.

In the *low fluence regime*, when the maximum temperature of the target stays below or close to T_c , the material ejection is limited to the evaporation of metal atoms from the surface of hot molten metal. The metal atoms evaporate into a low-density region formed at the plume-liquid interface and rapidly assemble into atomic clusters and small

Fig. 30 Schematic diagram summarizing the connections between the fluence regimes of laser ablation and the mechanisms of NP formation in PLAL



NPs with sizes below 1.5 nm. Below the continuous molten surface layer of the target, a transient appearance of sub-surface voids or a spongy structure of interconnected liquid regions is observed and attributed to a combined effect of the unloading of laser-induced pressure and an internal release of vapor in the part of the target superheated close to T_c . The sub-surface voids and the spongy structure rapidly collapse, as the top metal layer is decelerated and pushed back to the target by the liquid environment.

In the *medium fluence regime*, the temperature of the surface region of the target exceeds T_c , and the dense metal layer accumulated at the interface with the liquid environment and connected to the target by a spongy structure of liquid regions becomes unstable against nanoscale roughening and decomposition into large ($D > 4$ nm) NPs. The generation of large NPs through the roughening and decomposition of the top part of the interfacial layer leads to a sharp increase in the total ablation yield and drastically changes the NP size distribution. Further increase in the laser fluence leads to the splitting of the ablation plume into two distinct high-density regions, a hot cloud of supercritical material accumulated near the interface with the liquid environment and a spongy structure of liquid regions connected to the target surface. The spongy structure collapses under pressure from the expanding supercritical region, while the phase decomposition of the upper part of the plume into vapor, atomic clusters, and liquid droplets contributes to the further increase in the ablation yield.

The transition to the *high fluence regime* is signified by the spreading of the supercritical plume throughout the emerging cavitation bubble at the early stage of the plume expansion. The formation of the spongy liquid structure near the surface of the target is suppressed by pressure exerted by the supercritical fluid, and the NP generation occurs primarily at the phase separation front propagating from the interface with the liquid environment toward the target surface. The phase separation front approximately follows the $0.8T_c$ isotherm and occurs simultaneously with intense redeposition of the ablation plume to the target surface. The density of the homogeneous part of the plume decreases due to the redeposition, leading to a decrease in the size of the NPs formed at the phase separation front.

For the fluence dependence of the ablation yield, the simulations predict a steep increase in the ablation yield in the medium fluence regime and a weakening of the dependence at higher fluences. This observation suggests, in agreement with experimental observations, that the energy efficiency of the NP generation (total NP yield per unit energy deposited by the laser pulse) reaches its maximum close to the threshold for the formation of the supercritical plume and decreases at higher fluences due to the massive redeposition of the transiently ejected material.

The NP size distributions are highly sensitive to the ablation mechanisms and exhibit different characteristics in the three fluence regimes revealed in the simulations. The increase of laser fluence from low to medium irradiation regime causes a transition from the generation of atomic clusters and small NPs through the evaporation – condensation mechanism to a broad mass-weighted size distributions dominated by large NPs with diameters ranging from 4 to 12 nm. Further increase in the absorbed laser fluence, however, eliminates the largest NPs and produces a narrower size distribution.

Some of the NPs generated at the interface between the ablation plume and the liquid environment, or propelled into the dense and cold liquid environment at the initial dynamic stage of the ablation process, are observed to undergo rapid quenching and solidification on the time-scale of nanoseconds. The quench rates on the order of 10^{12} K/s bring the molten NPs into a state of deep undercooling and trigger rapid far-from-equilibrium solidification that produces NPs with high densities of crystal defects. The defect-rich NPs are highly desired for applications in catalysis, where the enhanced activity of NPs generated by PLAL is attributed to the elastic strain and surface states associated with crystal defects.

Finally, the results of the simulations performed with different absorbed laser fluences are mapped to local fluences realized within a laser spot irradiated by a beam with a Gaussian spatial profile. In this case, all the mechanisms of the material ejection and NP formation identified in the atomistic simulations are activated simultaneously in different parts of the Gaussian laser spot and are collectively contributing to the ablation yield and NP generation. The spatially and time-resolved maps of the transient nonequilibrium states predicted in the simulations provide a comprehensive picture of the ablation dynamics and a solid foundation for interpretation of the results of time-resolved experimental probing of the initial stage of the PLAL process. The consideration of the ablation process at the scale of the whole laser spot also enables evaluation of the fluence dependence of the ablation yield and the energy efficiency of the NP synthesis by laser beams with Gaussian spatial beam profiles. The computational predictions are found to be in good quantitative agreement with experimental observations, thus supporting the notion that the initial ablation dynamics explored in the atomistic simulations plays a key role in defining the final outcomes of the NPs synthesis by PLAL.

Acknowledgements Financial support for this work was provided by the U.S. Department of Energy, Office of Science, Basic Energy Sciences under contract number DE-SC0019191, as well as the National Science Foundation (NSF) through grants CMMI-1663429 and CBET-2126785. Leonid V. Zhigilei also acknowledges the Research Award of

the Alexander von Humboldt Foundation. Computational support was provided by the NSF through the Extreme Science and Engineering Discovery Environment (Grant No. TGDMR110090).

Data availability Data supporting this study are included within the article. Some of the datasets are available from the authors upon a reasonable request.

References

1. Special issue on nanoparticles in catalysis. *Chem. Rev.* **120**(2), 461–1512 (2020)
2. R.C. Forsythe, C.P. Cox, M.K. Wilsey, A.M. Müller, Pulsed laser in liquids made nanomaterials for catalysis. *Chem. Rev.* **121**, 7568–7637 (2021)
3. M.-C. Daniel, D. Astruc, Gold nanoparticles: Assembly, supramolecular chemistry, quantum-size-related properties, and applications toward biology, catalysis, and nanotechnology. *Chem. Rev.* **104**, 293–346 (2004)
4. C.M. Hussain (ed.), *Handbook of Nanomaterials for Industrial Applications* (Elsevier, Amsterdam, 2020)
5. J.H. Martin, B.D. Yahata, J.M. Hundley, J.A. Mayer, T.A. Schaedler, T.M. Pollock, 3D printing of high-strength aluminium alloys. *Nature* **549**, 365–369 (2017)
6. C. Doñate-Buendia, P. Kürnsteiner, F. Stern, M.B. Wilms, R. Streubel, I.M. Kusoglu, J. Tenkamp, E. Bruder, N. Pirch, S. Barcikowski, K. Durst, J.H. Schleifenbaum, F. Walther, B. Gault, B. Gökce, Microstructure formation and mechanical properties of ODS steels built by laser additive manufacturing of nanoparticle coated iron-chromium powders. *Acta Mater.* **206**, 116566 (2021)
7. D. Zhang, B. Gökce, Perspective of laser-prototyping nanoparticle-polymer composites. *Appl. Surf. Sci.* **392**, 991–1003 (2017)
8. O. Neumann, A.S. Urban, J. Day, S. Lal, P. Nordlander, N.J. Halas, Solar vapor generation enabled by nanoparticles. *ACS Nano* **7**, 42–49 (2013)
9. L. Zhang, J. Xing, X. Wen, J. Chai, S. Wang, Q. Xiong, Plasmonic heating from indium nanoparticles on a floating microporous membrane for enhanced solar seawater desalination. *Nanoscale* **9**, 12843–12849 (2017)
10. J.L. West, N.J. Halas, Engineered nanomaterials for biophotonics applications: improving sensing, imaging, and therapeutics. *Annu. Rev. Biomed. Eng.* **5**, 285–292 (2003)
11. N.G. Khlebtsov, L.A. Dykman, Optical properties and biomedical applications of plasmonic nanoparticles. *J. Quant. Spectrosc. Radiat. Transf.* **111**, 1–35 (2010)
12. D. Kim, K. Shin, S.G. Kwon, T. Hyeon, Synthesis and biomedical applications of multifunctional nanoparticles. *Adv. Mater.* **30**, 1802309 (2018)
13. K. Kaefer, K. Krüger, F. Schlapp, H. Uzun, S. Celiksoy, B. Flietel, A. Heimann, T. Schroeder, O. Kempfski, C. Sönnichsen, Implantable sensors based on gold nanoparticles for continuous long-term concentration monitoring in the body. *Nano Lett.* **21**, 3325–3330 (2021)
14. D. Zhang, B. Gökce, S. Barcikowski, Laser synthesis and processing of colloids: Fundamentals and applications. *Chem. Rev.* **117**, 3990–4103 (2017)
15. V. Amendola, D. Amans, Y. Ishikawa, N. Koshizaki, S. Scirè, G. Compagnini, S. Reichenberger, S. Barcikowski, Room-temperature laser synthesis in liquid of oxide, metal-oxide core-shells, and doped oxide nanoparticles. *Chem. Eur. J.* **26**, 9206–9242 (2020)
16. S. Jendrzzej, B. Gökce, M. Epple, S. Barcikowski, How size determines the value of gold: Economic aspects of wet chemical and laser-based metal colloid synthesis. *ChemPhysChem* **18**, 1012–1019 (2017)
17. C.-Y. Shih, R. Streubel, J. Heberle, A. Letzel, M.V. Shugaev, C. Wu, M. Schmidt, B. Gökce, S. Barcikowski, L.V. Zhigilei, Two mechanisms of nanoparticle generation in picosecond laser ablation in liquids: the origin of the bimodal size distribution. *Nanoscale* **10**, 6900–6910 (2018)
18. C.-Y. Shih, M.V. Shugaev, C. Wu, L.V. Zhigilei, Generation of subsurface voids, incubation effect, and formation of nanoparticles in short pulse laser interactions with bulk metal targets in liquid: Molecular dynamics study. *J. Phys. Chem. C* **121**, 16549–16567 (2017)
19. W. Huang, A.C. Johnston-Peck, T. Wolter, W.C.D. Yang, L. Xu, J. Oh, B.A. Reeves, C. Zhou, M.E. Holtz, A.A. Herzing, A.M. Lindenberg, M. Mavrikakis, M. Cargnello, Steam-created grain boundaries for methane C-H activation in palladium catalysts. *Science* **373**, 1518–1523 (2021)
20. Z. Li, J.-Y. Fu, Y. Feng, C.-K. Dong, H. Liu, X.-W. Du, A silver catalyst activated by stacking faults for the hydrogen evolution reaction. *Nat. Catal.* **2**, 1107–1114 (2019)
21. J.-Y. Lin, C. Xi, Z. Li, Y. Feng, D.-Y. Wu, C.-K. Dong, P. Yao, H. Liu, X.-W. Du, Lattice-strained palladium nanoparticles as active catalysts for the oxygen reduction reaction. *Chem. Commun.* **55**, 3121–3123 (2019)
22. Q. Lin, R. Nadarajah, E. Høglund, A. Semisalova, J.M. Howe, B. Gökce, G. Zangari, Towards synthetic $\text{Li}_0\text{-FeNi}$: Detecting the absence of cubic symmetry in laser-ablated Fe-Ni nanoparticles. *Appl. Surf. Sci.* **567**, 150664 (2021)
23. S. Reichenberger, Freezing crystallographic defects into nanoparticles: The development of pulsed laser defect engineering in liquid (PUDEL). *Sci. China: Phys. Mech. Astron.* **65**, 274208 (2022)
24. P. Wagener, S. Ibrahimkutty, A. Menzel, A. Plech, S. Barcikowski, Dynamics of silver nanoparticle formation and agglomeration inside the cavitation bubble after pulsed laser ablation in liquid. *Phys. Chem. Chem. Phys.* **15**, 3068–3074 (2013)
25. S. Ibrahimkutty, P. Wagener, T.D. Rolo, D. Karpov, A. Menzel, T. Braumbach, S. Barcikowski, A. Plech, A hierarchical view on material formation during pulsed-laser synthesis of nanoparticles in liquid. *Sci. Rep.* **5**, 16313 (2015)
26. A. Letzel, B. Gökce, P. Wagener, S. Ibrahimkutty, A. Menzel, A. Plech, S. Barcikowski, Size quenching during laser synthesis of colloids happens already in the vapor phase of the cavitation bubble. *J. Phys. Chem. C* **121**, 5356–5365 (2017)
27. K. Ando, T. Nakajima, Clear observation of the formation of nanoparticles inside the ablation bubble through a laser-induced flat transparent window by laser scattering. *Nanoscale* **12**, 9640–9646 (2020)
28. S. Reich, A. Letzel, A. Menzel, N. Kretzschmar, B. Gökce, S. Barcikowski, A. Plech, Early appearance of crystalline nanoparticles in pulsed laser ablation in liquids dynamics. *Nanoscale* **11**, 6962–6969 (2019)
29. M. Spellaugue, C. Doñate-Buendía, S. Barcikowski, B. Gökce, H.P. Huber, Comparison of ultrashort pulse ablation of gold in air and water by time-resolved experiments. *Light Sci. Appl.* **11**, 68 (2022)
30. M.E. Povarnitsyn, T.E. Itina, P.R. Levashov, K.V. Khishchenko, Mechanisms of nanoparticle formation by ultra-short laser ablation of metals in liquid environment. *Phys. Chem. Chem. Phys.* **15**, 3108–3114 (2013)
31. C.-Y. Shih, C. Wu, M.V. Shugaev, L.V. Zhigilei, Atomistic modeling of nanoparticle generation in short pulse laser ablation of thin metal films in water. *J. Colloid Interface Sci.* **489**, 3–17 (2017)

32. C.-Y. Shih, M.V. Shugaev, C. Wu, L.V. Zhigilei, The effect of pulse duration on nanoparticle generation in pulsed laser ablation in liquids: Insights from large-scale atomistic simulations. *Phys. Chem. Chem. Phys.* **22**, 7077–7099 (2020)
33. N.A. Inogamov, V.A. Khokhlov, Yu.V. Petrov, V.V. Zhakhovsky, Hydrodynamic and molecular-dynamics modeling of laser ablation in liquid: from surface melting till bubble formation. *Opt. Quantum Electron.* **52**, 63 (2020)
34. D.S. Ivanov, T. Izgin, A.N. Maiorov, V.P. Veiko, B. Rethfeld, Y.I. Dombrovska, M.E. Garcia, I.N. Zavestovskaya, S.M. Klimentov, A.V. Kabashin, Numerical investigation of ultrashort laser-ablative synthesis of metal nanoparticles in liquids using the atomistic-continuum model. *Molecules* **25**, 67 (2020)
35. C.-Y. Shih, C. Chen, C. Rehbock, A. Tymoczko, U. Wiedwald, M. Kamp, U. Schuermann, L. Kienle, S. Barcikowski, L.V. Zhigilei, Limited elemental mixing in nanoparticles generated by ultrashort pulse laser ablation of AgCu bilayer thin films in a liquid environment: atomistic modeling and experiments. *J. Phys. Chem. C* **125**, 2132–2155 (2021)
36. N.A. Inogamov, V.V. Zhakhovsky, V.A. Khokhlov, Physical processes accompanying laser ablation in liquid. *JETP Lett.* **115**, 16–22 (2022)
37. C. Chen, L.V. Zhigilei, Ultrashort pulse laser ablation in liquids: probing the first nanoseconds of underwater phase explosion. *Light Sci. Appl.* **11**, 111 (2022)
38. T.E. Itina, On nanoparticle formation by laser ablation in liquids. *J. Phys. Chem. C* **115**, 5044–5048 (2011)
39. V. Amendola, M. Meneghetti, What controls the composition and the structure of nanomaterials generated by laser ablation in liquid solution? *Phys. Chem. Chem. Phys.* **15**, 3027–3046 (2013)
40. M. Dell’Aglia, R. Gaudio, O. De Pascale, A. De Giacomo, Mechanisms and processes of pulsed laser ablation in liquids during nanoparticle production. *Appl. Surf. Sci.* **348**, 4–9 (2015)
41. T. Tsuji, Y. Okazaki, Y. Tsuboi, M. Tsuji, Nanosecond time-resolved observations of laser ablation of silver in water. *Jpn. J. Appl. Phys.* **46**, 1533–1535 (2007)
42. N. Lasemi, U. Pacher, L.V. Zhigilei, O. Bomati-Miguel, R. Lahoz, W. Kautek, Pulsed laser ablation and incubation of nickel, iron and tungsten in liquids and air. *Appl. Surf. Sci.* **433**, 772–779 (2018)
43. A.V. Kabashin, M. Meunier, Synthesis of colloidal nanoparticles during femtosecond laser ablation of gold in water. *J. Appl. Phys.* **94**, 7941–7943 (2003)
44. J.-P. Sylvestre, A.V. Kabashin, E. Sacher, M. Meunier, Femtosecond laser ablation of gold in water: influence of the laser-produced plasma on the nanoparticle size distribution. *Appl. Phys. A* **80**, 753–758 (2005)
45. L. Gamrad, C. Rehbock, J. Krawinkel, B. Tumursukh, A. Heisterkamp, S. Barcikowski, Charge balancing of model gold-nanoparticle-peptide conjugates controlled by the peptide’s net charge and the ligand to nanoparticle ratio. *J. Phys. Chem. C* **118**, 10302–10313 (2014)
46. G. Marzun, J. Nakamura, X. Zhang, S. Barcikowski, P. Wagener, Size control and supporting of palladium nanoparticles made by laser ablation in saline solution as a facile route to heterogeneous catalysts. *Appl. Surf. Sci.* **348**, 75–84 (2015)
47. S. Dittrich, S. Barcikowski, B. Gökce, Plasma and nanoparticle shielding during pulsed laser ablation in liquids cause ablation efficiency decrease. *Opto-Electron. Adv.* **4**, 200072 (2021)
48. C.-Y. Shih, I. Gnilitzkiy, M.V. Shugaev, E. Skoulas, E. Stratakis, L.V. Zhigilei, Effect of liquid environment on single-pulse generation of laser induced periodic surface structures and nanoparticles. *Nanoscale* **12**, 7674–7687 (2020)
49. M.V. Shugaev, C.-Y. Shih, E.T. Karim, C. Wu, L.V. Zhigilei, Generation of nanocrystalline surface layer in short pulse laser processing of metal targets under conditions of spatial confinement by solid or liquid overlayer. *Appl. Surf. Sci.* **417**, 54–63 (2017)
50. N. Tchipev, S. Seckler, M. Heinen, J. Vrabec, F. Gratl, M. Horsch, M. Bernreuther, C.W. Glass, C. Niethammer, N. Hammer, B. Krischok, M. Resch, D. Kranzlmüller, H. Hasse, H.-J. Bungartz, P. Neumann, TweTriS: twenty trillion-atom simulation. *Int. J. High Perform. Comput. Appl.* **33**, 838–854 (2019)
51. H. Watanabe, M. Suzuki, N. Ito, Huge-scale molecular dynamics simulation of multibubble nuclei. *Comput. Phys. Commun.* **184**, 2775–2784 (2013)
52. G. Chu, Y. Li, R. Zhao, S. Ren, W. Yang, X. He, C. Hu, J. Wang, MD simulation of hundred-billion-metal-atom cascade collision on Sunway Taihulight. *Comput. Phys. Commun.* **269**, 108128 (2021)
53. C. Wu, L.V. Zhigilei, Microscopic mechanisms of laser spallation and ablation of metal targets from large-scale molecular dynamics simulations. *Appl. Phys. A* **114**, 11–32 (2014)
54. V.P. Skripov, *Metastable Liquids* (Wiley, Israel Program for Scientific Translations, New York, 1974)
55. A. Miotello, R. Kelly, Laser-induced phase explosion: new physical problems when a condensed phase approaches the thermodynamic critical temperature. *Appl. Phys. A* **69**, S67–S73 (1999)
56. M.V. Shugaev, M. He, Y. Levy, A. Mazzi, A. Miotello, N.M. Bulgakova, L.V. Zhigilei, Laser-induced thermal processes: Heat transfer, generation of stresses, melting and solidification, vaporization and phase explosion, in *Handbook of Laser Micro- and Nano-Engineering*, ed. by K. Sugioka (Springer, Cham, 2021), pp.83–163
57. D.S. Ivanov, L.V. Zhigilei, Combined atomistic-continuum modeling of short-pulse laser melting and disintegration of metal films. *Phys. Rev. B* **68**, 064114 (2003)
58. M.V. Shugaev, M. He, S.A. Lizunov, Y. Levy, T.J.-Y. Derrien, V.P. Zhukov, N.M. Bulgakova, L.V. Zhigilei, Insights into laser-materials interaction through modeling on atomic and macroscopic scales, in *Advances in the Application of Lasers in Materials Science, Springer Series in Materials Science*, vol. 274, ed. by P.M. Ossi (Springer International Publishing Switzerland, 2018), pp.107–148
59. C. Schäfer, H.M. Urbassek, L.V. Zhigilei, B.J. Garrison, Pressure-transmitting boundary conditions for molecular-dynamics simulations. *Comp. Mater. Sci.* **24**, 421–429 (2002)
60. M. Tabetah, A. Matei, C. Constantinescu, N.P. Mortensen, M. Dinescu, J. Schou, L.V. Zhigilei, The minimum amount of “matrix” needed for matrix-assisted pulsed laser deposition of biomolecules. *J. Phys. Chem. B* **118**, 13290–13299 (2014)
61. J. Zou, C. Wu, W.D. Robertson, L.V. Zhigilei, R.J.D. Miller, Molecular dynamics investigation of desorption and ion separation following picosecond infrared laser (PIRL) ablation of an ionic aqueous protein solution. *J. Chem. Phys.* **145**, 204202 (2016)
62. Z. Lin, L.V. Zhigilei, V. Celli, Electron-phonon coupling and electron heat capacity of metals under conditions of strong electron-phonon nonequilibrium. *Phys. Rev. B* **77**, 075133 (2008)
63. Z. Lin, L.V. Zhigilei, Temperature dependences of the electron-phonon coupling, electron heat capacity and thermal conductivity in Ni under femtosecond laser irradiation. *Appl. Surf. Sci.* **253**, 6295–6300 (2007)
64. M. He, C. Wu, M.V. Shugaev, G.D. Samolyuk, L.V. Zhigilei, Computational study of short-pulse laser-induced generation of crystal defects in Ni-based single-phase binary solid-solution alloys. *J. Phys. Chem. C* **123**, 2202–2215 (2019)
65. G. Bonny, D. Terentyev, R.C. Pasianot, S. Poncé, A. Bakaev, Interatomic potential to study plasticity in stainless steels: The FeNiCr model alloy. *Model. Simul. Mater. Sci. Eng.* **19**, 085008 (2011)

66. Z. Wu, H. Bei, G.M. Pharr, E.P. George, Temperature dependence of the mechanical properties of equiatomic solid solution alloys with face-centered cubic crystal structures. *Acta Mater.* **81**, 428–441 (2014)
67. H. Okumura, F. Yonezawa, Reliable determination of the liquid–vapor critical point by the NVT plus test particle method. *J. Phys. Soc. Jpn.* **70**, 1990–1994 (2001)
68. D.S. Gates, G. Thodos, The critical constants of the elements. *AIChE J.* **6**, 50–54 (1960)
69. J. Drelich, E. Chibowski, D.D. Meng, K. Terpilowski, Hydrophilic and superhydrophilic surfaces and materials. *Soft Matter* **7**, 9804–9828 (2011)
70. N.R. Pallas, B.A. Pethica, The surface tension of water. *Colloids Surf.* **6**, 221–227 (1983)
71. T. Xiang, S. Ding, C. Li, S. Zheng, W. Hu, J. Wang, P. Liu, Effect of current density on wettability and corrosion resistance of superhydrophobic nickel coating deposited on low carbon steel. *Mater. Des.* **114**, 65–72 (2017)
72. S. Riahi, B. Niroumand, A.D. Moghadam, P.K. Rohatgi, Effect of microstructure and surface features on wetting angle of a Fe-3.2wt% C.E. cast iron with water. *Appl. Surf. Sci.* **440**, 341–350 (2018)
73. T. Halicioğlu, G.M. Pound, Calculation of potential energy parameters from crystalline state properties. *Phys. Status Solidi* **30**, 619–623 (1975)
74. S. Reich, J. Göttlicher, A. Ziefuss, R. Streubel, A. Letzel, A. Menzel, O. Mathon, S. Pascarelli, T. Baumbach, M. Zuber, B. Gökce, S. Barcikowski, A. Plech, *In situ* speciation and spatial mapping of Zn products during pulsed laser ablation in liquids (PLAL) by combined synchrotron methods. *Nanoscale* **12**, 14011–14020 (2020)
75. R. J. LeVeque, Numerical methods for conservation laws. In: *Lectures in Mathematics*, Vol. 132 (Springer, 1992).
76. H. Hu, T. Liu, H. Zhai, Comparison of femtosecond laser ablation of aluminum in water and in air by time-resolved optical diagnosis. *Opt. Express* **23**, 628–635 (2015)
77. E.D. Palik, *Handbook of Optical Constants of Solids* (Academic Press, New York, 1998)
78. Y. Zhang, G.M. Stocks, K. Jin, C. Lu, H. Bei, B.C. Sales, L. Wang, L.K. Béland, R.E. Stoller, G.D. Samolyuk, M. Caro, A. Caro, W.J. Weber, Influence of chemical disorder on energy dissipation and defect evolution in concentrated solid solution alloys. *Nat. Commun.* **6**, 8736 (2015)
79. E. Leveugle, D.S. Ivanov, L.V. Zhigilei, Photomechanical spallation of molecular and metal targets: molecular dynamics study. *Appl. Phys. A* **79**, 1643–1655 (2004)
80. M.V. Shugaev, L.V. Zhigilei, Thermodynamic analysis and atomistic modeling of subsurface cavitation in photomechanical spallation. *Comput. Mater. Sci.* **166**, 311–317 (2019)
81. L.V. Zhigilei, Z. Lin, D.S. Ivanov, Atomistic modeling of short pulse laser ablation of metals: Connections between melting, spallation, and phase explosion. *J. Phys. Chem. C* **113**, 11892–11906 (2009)
82. H. Huang, L.V. Zhigilei, Atomistic view of laser fragmentation of gold nanoparticles in a liquid environment. *J. Phys. Chem. C* **125**, 13413–13432 (2021)
83. P. Carlès, A brief review of the thermophysical properties of supercritical fluids. *J. Supercrit. Fluids* **53**, 2–11 (2010)
84. J.D. Honeycutt, H.C. Andersen, Molecular dynamics study of melting and freezing of small Lennard-Jones clusters. *J. Phys. Chem.* **91**, 4950–4963 (1987)
85. A. Stukowski, Visualization and analysis of atomistic simulation data with OVITO—the Open Visualization Tool. *Model. Simul. Mater. Sci. Eng.* **18**, 015012 (2009)
86. G. Rossi, R. Ferrando, Freezing of gold nanoclusters into polydecahedral structures. *Nanotechnology* **18**, 225706 (2007)
87. C.C. Asuquo, R.K. Bowles, Molecular dynamics simulations of competitive freezing in gold nanoclusters. *J. Phys. Chem. C* **116**, 14619–14626 (2012)
88. C. Wu, L.V. Zhigilei, Nanocrystalline and polyicosahedral structure of a nanospire generated on metal surface irradiated by a single femtosecond laser pulse. *J. Phys. Chem. C* **120**, 4438–4447 (2016)
89. V.G. Gryaznov, J. Heydenreich, A.M. Kaprelov, S.A. Nepijko, A.E. Romanov, J. Urban, Pentagonal symmetry and disclinations in small particles. *Cryst. Res. Technol.* **34**, 1091–1119 (1999)
90. A.E. Romanov, A.L. Kolesnikova, Application of disclination concept to solid structures. *Prog. Mater. Sci.* **54**, 740–769 (2009)
91. S. Dittrich, R. Streubel, C. McDonnell, H.P. Huber, S. Barcikowski, B. Gökce, Comparison of the productivity and ablation efficiency of different laser classes for laser ablation of gold in water and air. *Appl. Phys. A* **125**, 432 (2019)
92. Y. Monsa, G. Gal, N. Lerner, I. Bar, A simple strategy for enhanced production of nanoparticles by laser ablation in liquids. *Nanotechnology* **31**, 235601 (2020)
93. A.R. Ziefuss, T. Steenbock, D. Benner, A. Plech, J. Göttlicher, M. Teubner, B. Grimm-Lebsanft, C. Rehbock, C. Comby-Zerbino, R. Antoine, D. Amans, I. Chakraborty, G. Bester, M. Nachev, B. Sures, M. Rübhausen, W.J. Parak, S. Barcikowski, Photoluminescence of fully inorganic colloidal gold nanocluster and their manipulation using surface charge effects. *Adv. Mater.* **33**, 2101549 (2021)
94. J. Teeriniemi, M. Melander, S. Lipasti, R. Hatz, K. Laasonen, Fe-Ni nanoparticles: a multiscale first-principles study to predict geometry, structure, and catalytic activity. *J. Phys. Chem. C* **121**, 1667–1674 (2017)
95. H. Rong, S. Ji, J. Zhang, D. Wang, Y. Li, Synthetic strategies of supported atomic clusters for heterogeneous catalysis. *Nat. Commun.* **11**, 5884 (2020)
96. D. Bäuerle, *Laser Processing and Chemistry*, 3rd edn. (Springer-Verlag, Berlin, 2000)
97. R.A. Schowengerdt, *Sensor Models (Chapter 3)*, in *Remote Sensing—Models and Methods for Image Processing*, 3rd edn. (Academic Press, Burlington, 2007), pp.75–125
98. Y. Ren, J.K. Chen, Y. Zhang, J. Huang, Ultrashort laser pulse energy deposition in metal films with phase changes. *Appl. Phys. Lett.* **98**, 191105 (2011)
99. R. Streubel, G. Bendt, B. Gökce, Pilot-scale synthesis of metal nanoparticles by high-speed pulsed laser ablation in liquids. *Nanotechnology* **27**, 205602 (2016)

Publisher's Note Springer Nature remains neutral with regard to jurisdictional claims in published maps and institutional affiliations.

Springer Nature or its licensor (e.g. a society or other partner) holds exclusive rights to this article under a publishing agreement with the author(s) or other rightsholder(s); author self-archiving of the accepted manuscript version of this article is solely governed by the terms of such publishing agreement and applicable law.